Journal of Computational Physics 229 (2010) 5820–5842

Contents lists available at ScienceDirect

Journal of Computational Physics

journal homepage: www.elsevier.com/locate/jcp

A robust implicit multigrid method for RANS equations with two-equation turbulence models

M. Wasserman [a], Y. Mor-Yossef [b,*], I. Yavneh [c], J.B. Greenberg [a]

[a] Faculty of Aerospace Engineering, Technion, Israel Institute of Technology, Haifa 32000, Israel
[b] Israeli CFD Center, Caesarea Industrial Park 38900, Israel
[c] Computer Science Department, Technion, Israel Institute of Technology, Haifa 32000, Israel

ARTICLE INFO

Article history:
Received 25 November 2009
Received in revised form 8 March 2010
Accepted 12 April 2010
Available online 18 April 2010

Keywords:
RANS
Turbulence model
Positivity preservation
Numerical stiffness
Source term
Multigrid

ABSTRACT

The design of a new, truly robust multigrid framework for the solution of steady-state Reynolds-Averaged Navier–Stokes (RANS) equations with two-equation turbulence models is presented. While the mean-flow equations and the turbulence model equations are advanced in time in a loosely-coupled manner, their multigrid cycling is strongly coupled (FC-MG). Thanks to the loosely-coupled approach, the unconditionally positive-convergent implicit time-integration scheme for two-equation turbulence models (UPC) is used. An improvement to the basic UPC scheme convergence characteristics is developed and its extension within the multigrid method is proposed. The resulting novel FC-MG-UPC algorithm is nearly free of artificial stabilizing techniques, leading to increased multigrid efficiency. To demonstrate the robustness of the proposed algorithm, it is applied to linear and non-linear two-equation turbulence models. Numerical experiments are conducted, simulating separated flow about the NACA4412 airfoil, transonic flow about the RAE2822 airfoil and internal flow through a plane asymmetric diffuser. Results obtained from numerical simulations demonstrate the strong consistency and case-independence of the method.

1. Introduction

Turbulent flow simulations employing the Reynolds-Averaged Navier–Stokes (RANS) equations are widely used in research, development, and design processes. Among the RANS turbulence models, the two-equation k-ω [1] and k-ϵ [2] closure models are most widely used since they are considered well-balanced in terms of computational requirements and physical rationale. Two-equation RANS turbulence models are based on transport equations for turbulence quantities (e.g., turbulence kinetic energy), which are positive because of the underlying physics. The equations consist of convective, diffusive, and source-term operators.

Despite their relatively simple mathematical representation, two-equation turbulence models present serious numerical difficulties, including convergence and positivity–preservation difficulties. The common argument is that the convergence difficulties arise mainly due to the strongly non-linear source term, having time scales that greatly differ from those of the convective and diffusive terms. Furthermore, in the process of convergence, non-physical solutions, namely negative values of the turbulence quantities, may appear even if the analytical solution exists and is analytically guaranteed to remain positive [3]. These difficulties dramatically deteriorate convergence rates of the overall flow solver, requiring several thousands of iterations to reach the desired convergence criterion.

* Corresponding author. Tel.: +972 4 6273463; fax: +972 4 6273460.
E-mail addresses: markw@tx.technion.ac.il (M. Wasserman), yairm@iscfdc.co.il (Y. Mor-Yossef), irad@cs.technion.ac.il (I. Yavneh), aer9801@aerodyne.technion.ac.il (J.B. Greenberg).

0021-9991/$ - see front matter © 2010 Elsevier Inc. All rights reserved.
doi:10.1016/j.jcp.2010.04.023

Therefore, one of the main challenges in modern computational fluid dynamics (CFD) lies in accelerating numerical methods for solving the mean-flow and turbulence model equations in cases where conventional methods are not optimal. One of the fastest acceleration means known today is use of multigrid methods (MG). MG methods accelerate convergence rates of numerical schemes by using a hierarchy of grids, based on the notion that certain numerical error modes are more efficiently treated on a coarse grid than on a fine grid. However, a coarse grid may only be used in conjunction with a finer one, requiring proper data transfer between successive grids.

MG methods rely on two basic principles: *smoothing* and *coarse grid correction (CGC)*. First, standard iterative methods (e.g., Gauss–Seidel) with good smoothing (that is, elimination of high spatial frequency modes) properties are used to treat non-smooth errors in the solution. Pre-smoothing is required because only a smooth error is well represented both on fine and coarse grids, while non-smooth errors exhibit aliasing on coarse grids, significantly reducing the efficiency of CGC [4]. After a smooth error is obtained on the finest grid where a solution is sought, relaxation continues on coarser grids which are achieved by eliminating every other grid line in each coordinate direction. A coarse grid relaxation is substantially (up to four times in 2D) cheaper than its fine-grid counterpart, and is also more efficient in eliminating errors which are relatively smooth on a finer grid. Thus, efficiency can be increased by transferring (*restricting*) some of the fine-grid iterations required for convergence, to a coarser grid, and interpolating (*prolongating*) the results, that is, applying a coarse grid correction, to advance the solution on the finest grid.

While MG methods are well defined in a mathematical sense [5,6], their efficient application for RANS equations with two-equation turbulence models is rather difficult. Among the barriers currently standing in the way of demonstrating an optimally efficient MG method for the RANS equations is the successful incorporation of turbulence transport equations in the multigrid framework [7]. There are two basic approaches to the incorporation of turbulence models in MG methods:

- Mean-flow multigrid (MF-MG)
- Fully-coupled multigrid (FC-MG)

In MF-MG [8–10], the mean-flow equations are solved on all grid levels, while the turbulence model equations are integrated only on the finest grid where a solution is sought, as in single-grid computations. In this approach, turbulence variables are simply injected onto coarser grids, where they are frozen. This allows bypassing numerical difficulties arising from the destabilizing effects of productive turbulence model source terms [11]. However, mean-flow equations convergence was proven to be highly influenced by turbulence model equations convergence [12]. Therefore, insufficient acceleration of the turbulence transport equations due to a partial use of single-grid computations in MF-MG may result in an overall reduced convergence rate, compared to fully-coupled multigrid.

An alternative to MF-MG, is the fully-coupled multigrid approach (FC-MG), in which both the mean-flow equations and the turbulence model equations are solved on all grid levels that are created in a multigrid framework. Although FC-MG is regarded as being more efficient in terms of convergence, its actual implementation is far from being straightforward. Usually, artificial stabilization techniques are used to damp numerical difficulties encountered in integration of turbulence transport equations on coarse grid levels of the MG solution. In early phases of the simulation, when the fine-grid residual is still large, the transferred fine-grid defects may be high. As a result, high mean-flow gradients may appear on coarse grid levels, with the potential of causing excessive productive turbulence model source terms. Moreover, accuracy of strongly non-linear source terms cannot be fully preserved on coarse grid levels, possibly leading to divergence or inaccurate coarse grid correction. To improve stability, the turbulence source terms are computed on the fine grid only, and then restricted onto coarser grid levels where they are frozen. This technique is commonly termed *source-term freezing* [13–18]. While it was shown to be robust, the downside of this technique is that defects stemming from frozen source-term contributions are not properly sampled on coarse grid levels, thus reducing the efficiency of multigrid as a solver.

The growth and decay of turbulence kinetic energy and dissipation are generally balanced thanks to a careful tailoring of the turbulence model equations. However, when multigrid is used, typical behavior of turbulence energy and dissipation on coarse grid levels are lost, and therefore strong singularities in the turbulence viscosity may appear. Hence, instead of applying source-term freezing, some researchers only employ *turbulence viscosity freezing* on coarse grid levels to increase stability of the coupling mechanism between the mean-flow and turbulence quantities [19,20].

Another stabilization technique, specified for supersonic and hypersonic flows where shock waves may occur is termed *residual damping*. Gerlinger et al. [21,22] introduced locally damped transfer operators for mean-flow residuals in the vicinity of shock waves (using a TVD shock sensor), in regions were fine-grid residuals may be inaccurately sampled on coarse grid levels. Damping is performed by applying an under relaxation coefficient in the MG restriction and/or prolongation phase, thus controlling the multigrid error correction rate. Obviously, in regions where this technique is used, coarse grid levels are less efficient for correcting fine-grid errors, since the forcing term in charge of driving the multigrid correction process is damped. Therefore, the overall convergence rate may not be optimal.

It has been shown that the highly non-linear nature of turbulence source terms leads to their inaccurate representation on coarse grid levels. Wackers and Koren [23] suggested the use of Galerkin operators as a means of circumventing this issue. Instead of reconstructing the fine-grid turbulence operators on coarse grids, the operators are projected to coarse grids, thus preventing instability due to inaccurate reconstruction of turbulence operators on coarse grids. This elegant approach was reported to yield good results for the simulation of RANS equations coupled with Menter's one-equation turbulence model.

However, since Galerkin operators can only be constructed efficiently for linear equations, a local time-linearization of fine-grid operators is required at each time step.

A successful multigrid algorithm that includes the solution of RANS turbulence model equations requires the use of a positive-preserving scheme. Positivity-preserving difficulties within MG may appear in the smoothing (relaxation) and prolongation stages. The positivity preserving difficulties of turbulence quantities in single-grid computations (or on the finest grid level of a multigrid hierarchy) are amplified on coarse grid levels. Inappropriate numerical treatment of turbulence equations may result in stall or divergence due to the appearance of non-physical values of turbulence quantities, leading to inefficient coarse grid correction and to the loss of multigrid robustness. Moreover, as the coarse grid correction can be negative, it is possible that the turbulence quantities on the fine-grid admit non-physical negative values. The common technique to avoid negative values of turbulence quantities in the prolongation stage is to employ artificial fixes [16,24] by either allowing only positive increments, or by locally neglecting corrections that cause loss of positivity. This guarantees that MG does not induce loss of positivity, but in regions where a coarse grid correction is neglected, convergence rates may deteriorate. In conclusion, while the above techniques increase stability of multigrid for the RANS equations coupled with two-equation turbulence models, they may also hinder convergence rates.

The present study focuses on designing a multigrid method for an implicit solver of the compressible RANS equations, together with a two-equation turbulence model. The work was guided by the belief that designing a robust multigrid method for this problem strongly depends on use of a highly stable scheme for the turbulence model equations. It was realized that some of the difficulties encountered in the multigrid solution of RANS turbulence models occur in fact due to the use of insufficiently stable relaxation schemes, rather than to the multigrid concept itself. Therefore, the unconditionally positive-convergent (UPC) time-integration implicit scheme for turbulence transport equations developed by Mor-Yossef and Levy [25] is adopted in this work and successfully extended for use in multigrid methods, allowing for smooth incorporation of these equations in a multigrid framework for the RANS equations. The proposed method is based on a full approximation storage (FAS) fully-coupled multigrid approach (FC-MG). The method is nearly free of stabilization fixes and other techniques commonly used to avoid numerical difficulties.

2. Governing equations

The governing equations are obtained by Favre-averaging the Navier–Stokes equations (RANS) and modeling the Reynolds stress. The unknown Favre-averaging Reynolds stress tensor is modeled in this work via linear or non-linear two-equation turbulence models. The linear model used is the k-ω turbulence model developed by Kok [26], which is considered to be topology-free and was designed to resolve the well-known dependency on free-stream values of ω. The non-linear model used is based on Kok's model together with the explicit algebraic Reynolds stress model (EARSM) developed by Wallin and Johansson [27]. Hereafter the linear and non-linear turbulence models are referred to as *kω-Linear* and *kω-EARSM*, respectively.

In a compact conservation law form, the 2D RANS equations may be expressed in Cartesian coordinates as follows:

$$\frac{\partial \boldsymbol{\mathcal{Q}}}{\partial t}+\frac{\partial(\boldsymbol{\mathcal{F}}_c-\boldsymbol{\mathcal{F}}_d)}{\partial x}+\frac{\partial(\boldsymbol{\mathcal{G}}_c-\boldsymbol{\mathcal{G}}_d)}{\partial y}=\boldsymbol{\mathcal{S}}. \tag{1}$$

The vector $\boldsymbol{\mathcal{Q}}=\{\mathbf{Q},\mathbf{q}\}$ denotes the dependent variables vector of mean-flow equations, $\mathbf{Q}$, and of the turbulence model equations, $\mathbf{q}$, given as

$$\mathbf{Q}=\begin{bmatrix}\rho\\ \rho u\\ \rho v\\ E\end{bmatrix},\quad \mathbf{q}=\begin{bmatrix}\rho k\\ \rho\omega\end{bmatrix}. \tag{2}$$

The fluid density is denoted by ρ, the Cartesian velocity vector components are denoted by u and v, and E denotes the total energy. The turbulence kinetic energy is denoted by k. The second turbulence quantity is denoted by ω, representing the specific turbulence dissipation rate. The convective flux vectors are denoted by $\boldsymbol{\mathcal{F}}_c=\{\mathbf{F}_c,\mathbf{f}_c\}$ and $\boldsymbol{\mathcal{G}}_c=\{\mathbf{G}_c,\mathbf{g}_c\}$, where $\mathbf{F}_c$, $\mathbf{G}_c$ and $\mathbf{f}_c$, $\mathbf{g}_c$ are the mean-flow and turbulence model equations convective flux vectors, respectively:

$$\mathbf{F}_c=\begin{bmatrix}\rho u\\ \rho uu+p\\ \rho uv\\ u(E+p)\end{bmatrix},\quad \mathbf{G}_c=\begin{bmatrix}\rho v\\ \rho uv\\ \rho v^2+p\\ v(E+p)\end{bmatrix}, \tag{3}$$

$$\mathbf{f}_c=\begin{bmatrix}\rho uk\\ \rho u\omega\end{bmatrix},\quad \mathbf{g}_c=\begin{bmatrix}\rho vk\\ \rho v\omega\end{bmatrix}. \tag{4}$$

The diffusive flux vectors are denoted as $\boldsymbol{\mathcal{F}}_d=\{\mathbf{F}_d,\mathbf{f}_d\}$ and $\boldsymbol{\mathcal{G}}_d=\{\mathbf{G}_d,\mathbf{g}_d\}$, where $\mathbf{F}_d$, $\mathbf{G}_d$ and $\mathbf{f}_d$, $\mathbf{g}_d$ are the mean-flow and turbulence model equations diffusive flux vectors, respectively:

$$\mathbf{F}_d = \begin{bmatrix} 0 \\ \tau_{xx} \\ \tau_{xy} \\ u\tau_{xx} + v\tau_{xy} + \kappa_d \frac{\partial T}{\partial x} \end{bmatrix}, \quad \mathbf{G}_d = \begin{bmatrix} 0 \\ \tau_{xy} \\ \tau_{yy} \\ u\tau_{xy} + v\tau_{yy} + \kappa_d \frac{\partial T}{\partial y} \end{bmatrix}, \tag{5}$$

$$\mathbf{f}_d = \begin{bmatrix} \mu_k \frac{\partial k}{\partial x} \\ \mu_\omega \frac{\partial \omega}{\partial x} \end{bmatrix}, \quad \mathbf{g}_d = \begin{bmatrix} \mu_k \frac{\partial k}{\partial y} \\ \mu_\omega \frac{\partial \omega}{\partial y} \end{bmatrix}. \tag{6}$$

The fluid temperature is denoted by T and $\kappa_d = \kappa_l + \kappa_t$ represents the thermal conductivity of the fluid with κ_l and κ_t being the molecular and turbulent thermal conductivity coefficients, respectively. The shear stresses are defined as

$$\tau_{xx} = 2(\mu + \mu_t)\frac{\partial u}{\partial x} - \frac{2}{3}(\mu + \mu_t)\left(\frac{\partial u}{\partial x} + \frac{\partial v}{\partial y}\right) - \frac{2}{3}\rho k + \psi\tau_{xx}^{nl}, \tag{7}$$

$$\tau_{yy} = 2(\mu + \mu_t)\frac{\partial v}{\partial y} - \frac{2}{3}(\mu + \mu_t)\left(\frac{\partial u}{\partial x} + \frac{\partial v}{\partial y}\right) - \frac{2}{3}\rho k + \psi\tau_{yy}^{nl}, \tag{8}$$

$$\tau_{xy} = (\mu + \mu_t)\left(\frac{\partial u}{\partial x} + \frac{\partial v}{\partial y}\right) + \psi\tau_{xy}^{nl}, \tag{9}$$

where τ_{xx}^{nl}, τ_{xy}^{nl}, and τ_{yy}^{nl} represent the supplementary high-order terms used in the EARSM model, and the scalar ψ distinguishes between the linear ($\psi = 0$) and non-linear ($\psi = 1$) models. The molecular viscosity, μ, is calculated from Sutherland's law, and μ_t denotes the turbulent viscosity. The turbulence diffusive flux vector coefficients μ_k,μ_ω are defined as

$$\mu_k = \mu + \frac{\mu_t}{\sigma_k}, \tag{10}$$

$$\mu_\omega = \mu + \frac{\mu_t}{\sigma_\omega}, \tag{11}$$

where σ_k,σ_ω are model-specific closure coefficients. The mean-flow equations are closed using the equation of state for a perfect gas, given by

$$p = \left[E - \frac{1}{2}\rho(u^2 + v^2)\right](\gamma - 1), \tag{12}$$

where γ is the ratio of specific heats (c_p/c_v), set to $\gamma = 1.4$. In the flows examined in this work, source terms appear only due to turbulence model equations. Therefore, the source-term vector $\mathcal{S}$ is represented by

$$\mathcal{S} = \begin{bmatrix} 0 \\ 0 \\ 0 \\ 0 \\ S_k \\ S_\omega \end{bmatrix}. \tag{13}$$

The source terms S_k,S_ω are given by

$$S_k = P_k - \beta^* \rho k \omega, \tag{14}$$

$$S_\omega = \alpha_\omega \frac{\omega}{k} P_k - \beta\rho\omega^2 + \sigma_d \frac{\rho}{\omega} \max\left(\frac{\partial k}{\partial x}\frac{\partial \omega}{\partial x} + \frac{\partial k}{\partial y}\frac{\partial \omega}{\partial y}, 0\right), \tag{15}$$

where P_k denotes the production term:

$$P_k = \mu_t\left\{2\left[\left(\frac{\partial u}{\partial x}\right)^2 + \left(\frac{\partial v}{\partial y}\right)^2\right] + \left(\frac{\partial u}{\partial y} + \frac{\partial v}{\partial x}\right)^2 - \frac{2}{3}\left(\frac{\partial u}{\partial x} + \frac{\partial v}{\partial y}\right)^2\right\} - \frac{2}{3}\left(\frac{\partial u}{\partial x} + \frac{\partial v}{\partial y}\right)\rho k + \psi\left[\tau_{xx}^{nl}\frac{\partial u}{\partial x} + \tau_{xy}^{nl}\left(\frac{\partial u}{\partial y} + \frac{\partial v}{\partial x}\right) + \tau_{yy}^{nl}\frac{\partial v}{\partial y}\right]. \tag{16}$$

A unified formulation of the turbulent viscosity of the linear and non-linear turbulence models is given in:

$$\mu_t = (1 - \psi)\frac{\rho k}{\omega} + \psi C_\mu \rho k \max\left(\frac{1}{\beta^* \omega},\ 6.0\frac{\sqrt{\mu}}{\sqrt{\beta^* k \omega \rho}}\right). \tag{17}$$

Detailed formulation of the high-order part of the Reynolds stress tensor, namely τ_{xx}^{nl}, τ_{xy}^{nl} and τ_{yy}^{nl}, and of the coefficient C_μ may be found in [27]. The remaining model-specific closure coefficients are given in Table 1.

Table 1
Turbulence models constants.

Model type	σ_k	σ_ω	σ_d	β	β^*	α_ω
kω-Linear	1.5	2.0	0.5	0.075	0.09	0.5531666
kω-EARSM	1.5	1.81	0.3	0.075	0.09	0.53

3. Numerical method

A conservative cell-centered finite volume methodology is employed to discretize the governing equations on structured grids. Let C_a denote the control area (defined by a grid area element), and let $\partial\Gamma$ denote the control area boundary, with $\mathbf{n} = [n_x, n_y]^T$ being the outward-pointing unit normal vector to $\partial\Gamma$. Therefore, the integral form of Eq. (1) for a control area C_a can be expressed as

$$\frac{\partial}{\partial t}\int_{C_a} \mathcal{Q} dA + \int_{\partial\Gamma} (\mathcal{H}_c - \mathcal{H}_d) dl = \int_{C_a} \mathcal{S} dA, \tag{18}$$

where $\mathcal{H}_c = \mathcal{F}_c n_x + \mathcal{G}_c n_y$, and $\mathcal{H}_d = \mathcal{F}_d n_x + \mathcal{G}_d n_y$.

3.1. Spatial discretization

The semi-discrete form of Eq. (18) for cell i of a non-deforming grid is given by

$$A_i \frac{d\mathcal{Q}_i}{dt} = -\sum_{j\in N(i)} \left(\mathcal{H}_{c_{ij}} - \mathcal{H}_{d_{ij}}\right) l_{ij} + \mathcal{S}_i A_i \equiv \mathcal{R}_i, \tag{19}$$

where $\mathcal{Q}_i$ is the vector of cell-averaged conservative variables, and $\mathcal{S}_i$ is the cell source vector. The terms $\mathcal{H}_{c_{ij}}$ and $\mathcal{H}_{d_{ij}}$ are the convective and diffusive fluxes, respectively, normal to the interface ij shared by cell i and its neighboring cell j. A_i is the cell area, and t represents the time. The term l_{ij} is the face length of the interface ij, and $N(i)$ denotes the set of cell i's neighbors (direct face neighbors). The vector $\mathcal{R}_i$ signifies the right-hand side (residual) of the equation set:

$$\mathcal{R}_i = \left\{\mathbf{R}^T, \mathbf{r}^T\right\}_i^T, \tag{20}$$

where $\mathbf{R}$ represents the residual of the mean-flow equations, and $\mathbf{r}$ represents the residual of the turbulence model equations.

The convective flux vector of the mean-flow equations is computed at the cell interface using the HLLC scheme proposed by Batten et al. [28]. The left and right state vectors of the convective flux are evaluated using a third-order bias MUSCL method, with the van Albada limiter [29] used to suppress oscillations in the solution. The diffusive flux vector of the mean-flow equations is discretized by employing central differencing based on the diamond stencil [30].

The convective flux vector of the turbulence model equations is computed based on the passive scalar approach [31], within the HLLC numerical framework [28]. The convective flux vector of the turbulence model equations, normal to the interface ij, is evaluated with first-order accuracy as follows:

$$(\mathbf{f}_c)_{ij} = \begin{cases} (U_n)_i \mathbf{q}_i, & S_L > 0, \\ \frac{S_L - (U_n)_i}{S_L - S_M} S_M \mathbf{q}_i, & S_L \leqslant 0 < S_M, \\ \frac{S_R - (U_n)_j}{S_R - S_M} S_M \mathbf{q}_j, & S_M \leqslant 0 \leqslant S_R, \\ (U_n)_j \mathbf{q}_j, & S_R < 0, \end{cases} \tag{21}$$

where U_n is the velocity normal to the interface ij, $U_n = un_x + vn_y$. The signal velocities S_L, S_R, and S_M are computed according to Ref. [28]. The turbulence model diffusive flux vector is evaluated according to the thin-layer approximation, namely:

$$(\mathbf{f}_d)_{ij} = \begin{bmatrix} \frac{\mu_k}{|\mathbf{d}\cdot\mathbf{n}|} & 0 \\ 0 & \frac{\mu_\omega}{|\mathbf{d}\cdot\mathbf{n}|} \end{bmatrix}_{ij} \left(\frac{1}{\rho_j}\mathbf{q}_j - \frac{1}{\rho_i}\mathbf{q}_i\right), \tag{22}$$

where $\mathbf{d}_{ij}$ is the distance vector between cell i and cell j centers.

3.2. Time integration

Implicit time marching of both the mean-flow, and the turbulence model discretized equations is employed, based on the first-order implicit backward Euler method:

$$\left[\frac{A}{\Delta t}\mathcal{I}-\frac{\partial \mathcal{R}}{\partial \mathcal{Q}}\right]^n \Delta \mathcal{Q}^n = \mathcal{R}^n, \tag{23}$$

where $\mathcal{I}$ is the identity matrix, and the Δ operator is defined as the increment between time levels n and $n+1$. Eq. (23) is solved using the alternating line symmetric Gauss–Seidel method, in a loosely-coupled manner. Namely, the implicit Jacobian is approximated as follows:

$$\left(\frac{\partial \mathcal{R}}{\partial \mathcal{Q}}\right)_{ij} = \begin{bmatrix} \left[\frac{\partial \mathbf{R}}{\partial \mathbf{Q}}\right]_{4\times 4}, & [0]_{4\times 2} \\ [0]_{2\times 4}, & \left[\frac{\partial \mathbf{r}}{\partial \mathbf{q}}\right]_{2\times 2} \end{bmatrix}_{ij}. \tag{24}$$

Loosely-coupled time-integration possesses several advantages over a coupled strategy. It is easy to implement and it provides the enhanced flexibility required to design a stable and efficient scheme for the turbulence model equations.

3.2.1. Mean-flow equations time integration

The algebraic set of the discretized mean-flow equations may be written as

$$\left[\frac{A}{\Delta t}\mathcal{I}-\frac{\partial \mathbf{R}}{\partial \mathbf{Q}}\right]^n \Delta \mathbf{Q}^n = \mathbf{R}^n. \tag{25}$$

The evaluation of the exact Jacobian $\frac{\partial \mathbf{R}}{\partial \mathbf{Q}}$, of the high-order, non-linear explicit operator $\mathbf{R}$ is very complicated. To alleviate this difficulty, the common practice is to approximate the Jacobian using the spatial lower-order accuracy of the explicit operator, meaning that the approximated Jacobian of the convective part is based on a first-order spatial accuracy of the convective explicit operator. The Jacobian of the diffusive part is based on the thin-layer approximation, namely, the approximated Jacobian is based on a compact stencil which takes into account only direct face neighbors. Moreover, the non-linear Reynolds-stress tensor that appears in the mean-flow equations is treated implicitly only with regard to its linear part. The remaining high-order terms, namely τ_{xx}^{nl}, τ_{xy}^{nl} and τ_{yy}^{nl}, are treated explicitly. In the current work, the approximated Jacobian of the mean-flow convective part is evaluated using the HLLC Jacobian by Batten et al. [28]. The diffusive part of the Jacobian is calculated analytically. An implicit treatment of boundary conditions is employed only for wall boundaries.

To improve iterative convergence to a steady-state solution, the B2 scheme proposed by Batten et al. [28] is used. The B2 scheme is a modified variant of the backward Euler time-integration method. Denoting the time integration given in Eq. (25) by

$$\Delta \mathbf{Q}^n = B1(\mathbf{Q}^n, \Delta t) \Rightarrow \mathbf{Q}^{n+1} = \mathbf{Q}^n + \Delta \mathbf{Q}^n, \tag{26}$$

the B2 scheme is defined as two successive modified B1 steps as follows:

$$\begin{aligned} &\text{1st step}: \Delta \mathbf{Q}^* = B1\left(\mathbf{Q}^n, \Delta t/2\right) \Rightarrow \mathbf{Q}^* = \mathbf{Q}^n + \Delta \mathbf{Q}^*, \\ &\text{2nd step}: \overline{\Delta \mathbf{Q}} = B1(\mathbf{Q}^*, \Delta t) \Rightarrow \mathbf{Q}^{n+1} = \mathbf{Q}^* + \overline{\Delta \mathbf{Q}}/2. \end{aligned} \tag{27}$$

As pointed out by Batten et al. [28], the B2 scheme may alleviate convergence difficulties that are associated with the high-frequency fluctuations of limiters.

3.2.2. Turbulence model equations time-integration method

Similarly to the algebraic set of the discretized mean-flow equations, the algebraic set of the discretized turbulence model equations is given by

$$\left[\frac{A}{\Delta t}\mathcal{I}-\frac{\partial \mathbf{r}}{\partial \mathbf{q}}\right]^n \Delta \mathbf{q}^n = \mathbf{r}^n. \tag{28}$$

A straightforward implementation of the turbulence model equations' exact Jacobian, $\frac{\partial \mathbf{r}}{\partial \mathbf{q}}$, usually leads to an unstable scheme that exhibits convergence and positivity-preserving difficulties. These numerical difficulties are even further amplified in a multigrid framework. As already mentioned, any lagging in the turbulence model time integration, with respect to that of the mean-flow equations, may hinder the convergence rate. Therefore, a highly stable implicit scheme for the turbulence model equations is vital for the success of FC-MG computations. It should be noted that the B2 scheme is not used for time integration of the turbulence model equations, and therefore Eq. (28) is employed only in the second step of the B2 scheme of the mean-flow equations.

In this work, the unconditionally positive-convergent (UPC) time integration implicit scheme for turbulence transport equations developed by Mor-Yossef and Levy [25] is adopted and successfully extended for use in multigrid methods. The key idea of the UPC scheme is the design of the implicit operator to form an M-matrix [32]. Specifically, the Jacobian, $-\frac{\partial \mathbf{r}}{\partial \mathbf{q}}$, is approximated by a matrix $\mathcal{M} \approx -\frac{\partial \mathbf{r}}{\partial \mathbf{q}}$ such that it fulfills the following two conditions:

1. $\mathcal{M}$ is an M-matrix
2. $\mathbf{r} + \mathcal{M}\mathbf{q}$ is a non-negative vector (i.e., all its entries are non-negative)

By substituting the matrix $\mathcal{M}$ for the matrix $-\frac{\partial \mathbf{r}}{\partial \mathbf{q}}$, Eq. (28) may be rewritten as

$$\left[\frac{A}{\Delta t}\mathcal{I}+\mathcal{M}\right]^n \Delta \mathbf{q}^n = \mathbf{r}^n, \tag{29}$$

Eq. (29) represents an unconditionally positive-convergent scheme. Complete details of the proof and construction may be found in Ref. [33].

Fig. 1 demonstrates the increased efficiency of a single-grid (SG) solver based on the UPC scheme, compared to a solver that is based on a standard implicit scheme for the turbulence equations. The flow simulation was conducted about the RAE2822 airfoil at $M_\infty = 0.734$, $Re_\infty = 6.5 \times 10^6$, and $\alpha = 2.54^\circ$ (referred to as case 9 in Ref. [34]), using the *kω-Linear* turbulence model and a 275 × 67 C-type grid. It can be seen that the use of the UPC scheme saves nearly 80% of the computational time that is required by a standard implicit scheme (measured in terms of WU-equivalent to a time step in a single-grid computation). Note that an infinite Courant–Friedrichs–Lewy (CFL) number was used for integrating the turbulence model equations (CFLT) with the UPC scheme, while only CFLT = 10 or less yielded stable results using the standard implicit scheme. Furthermore, thanks to the UPC scheme, CFL numbers as high as CFL = 200 were allowed for the mean-flow equations, while a standard implicit scheme converged only with CFL = 100 or less for the mean-flow equations. This clearly demonstrates the significant contribution of the UPC scheme to the basic flow solver robustness.

In Ref. [33] the diffusive implicit operator was designed in a similar manner to the convective implicit operator. However, in this work, a further improvement to the scheme with regard to the diffusive implicit operator is presented. The motivation in reconstruction of the implicit diffusive operator was to achieve a form as close as possible to the exact discrete Jacobian, while still guaranteeing the positivity of the turbulence quantities. Let the vector $\mathbf{r}_{d_i}$ denote the turbulence diffusive flux vector, given by

$$\mathbf{r}_{d_i} = \sum_{j\in N(i)} \mathbf{f}_{d_{ij}} l_{ij} = \sum_{j\in N(i)} \mathcal{D}^i_{ij}\mathbf{q}_i + \sum_{j\in N(i)} \mathcal{D}^j_{ij}\mathbf{q}_j. \tag{30}$$

For the thin-layer approximation, the matrix $\mathcal{D}^i_{ij}$ is defined as

$$\mathcal{D}^i_{ij} = -\frac{l_{ij}}{\rho_i}\begin{bmatrix} \left(\frac{\mu_k}{|\mathbf{d}\cdot\mathbf{n}|}\right) & 0 \\ 0 & \left(\frac{\mu_\omega}{|\mathbf{d}\cdot\mathbf{n}|}\right) \end{bmatrix}_{ij}, \tag{31}$$

and the matrix $\mathcal{D}^j_{ij}$ is defined as

$$\mathcal{D}^j_{ij} = \frac{l_{ij}}{\rho_j}\begin{bmatrix} \left(\frac{\mu_k}{|\mathbf{d}\cdot\mathbf{n}|}\right) & 0 \\ 0 & \left(\frac{\mu_\omega}{|\mathbf{d}\cdot\mathbf{n}|}\right) \end{bmatrix}_{ij} = -\frac{\rho_i}{\rho_j}\mathcal{D}^i_{ij}. \tag{32}$$

It can be seen that the differences between the matrices $\mathcal{D}^i_{ij}$ and $\mathcal{D}^j_{ij}$ stem from compressibility effects ($\rho_i \neq \rho_j$). Based on this observation, the turbulence diffusive flux vector may be recast as follows:

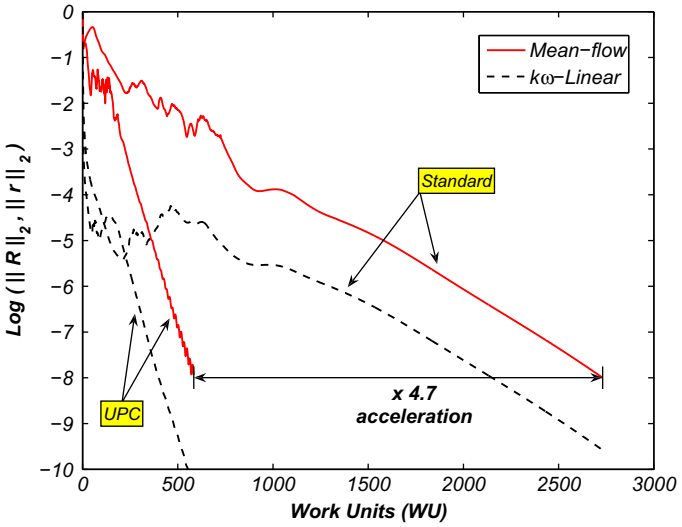

Fig. 1. Comparison of single-grid (SG) convergence histories for simulating flow about the RAE2822 airfoil at $M_\infty = 0.734$, $Re_\infty = 6.5 \times 10^6$, and $\alpha = 2.54^\circ$ (referred to as case 9 in Ref. [34]), using a 275 × 67 C-type grid. UPC (CFL = 200, CFLT = ∞) vs. Standard (CFL = 100, CFLT = 10).

$$\mathbf{r}_{d_i} = \sum_{j\in N(i)} \mathcal{D}^i_{ij}(\mathbf{q}_i - \mathbf{q}_j) + \sum_{j\in N(i)} \rho_j \left(\frac{1}{\rho_j} - \frac{1}{\rho_i}\right) \mathcal{D}^j_{ij}\mathbf{q}_j. \tag{33}$$

To simplify the construction of the implicit Jacobian, each of the matrices $\mathcal{D}^i_{ij}, \mathcal{D}^j_{ij}$, are split into their positive and negative parts. Let the matrix $\mathcal{A} = (a_{kl} \in R^{2\times 2})$ denote any of the matrices $\mathcal{D}^i_{ij}$, and $\mathcal{D}^j_{ij}$. Then a matrix $\mathcal{A}$ can be split into its positive and negative parts as follows:

$$\mathcal{A} = \mathcal{A}_P - \mathcal{A}_N, \tag{34}$$

where the matrices $\mathcal{A}_P = ((a_P)_{kl} \in R^{2\times 2})$ and $\mathcal{A}_N = ((a_N)_{kl} \in R^{2\times 2})$ are defined as

$$(a_P)_{kl} = \frac{1}{2}(|a_{kl}| + a_{kl}), \tag{35}$$

$$(a_N)_{kl} = \frac{1}{2}(|a_{kl}| - a_{kl}). \tag{36}$$

Then the turbulence diffusive residual can be rewritten in terms of the positive and negative parts appropriately:

$$\mathbf{r}_{d_i} = \sum_{j\in N(i)} \left[\left(\mathcal{D}^i_{ij}\right)_P - \left(\mathcal{D}^i_{ij}\right)_N\right](\mathbf{q}_i - \mathbf{q}_j) + \sum_{j\in N(i)} \rho_j[\delta_P - \delta_N]\left[\left(\mathcal{D}^j_{ij}\right)_P - \left(\mathcal{D}^j_{ij}\right)_N\right]\mathbf{q}_j, \tag{37}$$

where δ_P and δ_N are defined as

$$\delta_P = \max\left(\frac{1}{\rho_j} - \frac{1}{\rho_i}, 0\right), \quad \delta_N = \max\left(\frac{1}{\rho_i} - \frac{1}{\rho_j}, 0\right) \tag{38}$$

Moreover, thanks to the thin-layer approximation, the matrices $(\mathcal{D}^i_{ij})_P$ and $(\mathcal{D}^j_{ij})_N$ are identically zero, hence, Eq. (37) becomes:

$$\mathbf{r}_{d_i} = \sum_{j\in N(i)} -\left(\mathcal{D}^i_{ij}\right)_N(\mathbf{q}_i - \mathbf{q}_j) + \sum_{j\in N(i)} \rho_j[\delta_P - \delta_N]\left(\mathcal{D}^j_{ij}\right)_P\mathbf{q}_j. \tag{39}$$

For the purpose of deriving the desired implicit operator appropriately, Eq. (39) is rearranged as follows:

$$\mathbf{r}_{d_i} = \sum_{j\in N(i)} \left[-\left(\mathcal{D}^i_{ij}\right)_N - \left[\rho_j\delta_N\left(\mathcal{D}^j_{ij}\right)_P\right]\mathcal{T}^i_j\right]\mathbf{q}_i + \sum_{j\in N(i)} \left\{\left[\rho_j\delta_P\left(\mathcal{D}^j_{ij}\right)_P + \left(\mathcal{D}^i_{ij}\right)_N\right]\right\}\mathbf{q}_j, \tag{40}$$

where the matrix $\mathcal{T}^i_j$ is defined as

$$\mathcal{T}^i_j = \begin{bmatrix} \frac{(\rho k)_j}{(\rho k)_i} & 0 \\ 0 & \frac{(\rho\omega)_j}{(\rho\omega)_i} \end{bmatrix}. \tag{41}$$

Denote the implicit diffusive operator part of $\mathcal{M}$ by the matrix $\mathcal{M}_d$. Let $(\mathcal{M}_d)_{ii}$ and $(\mathcal{M}_d)_{ij}$ be the diagonal and off-diagonal block matrices of row i of the matrix $\mathcal{M}_d$, respectively. Then, they are proposed to be evaluated as follows:

$$(\mathcal{M}_d)_{ii} = \sum_{j\in N(i)} \left[\left(\mathcal{D}^i_{ij}\right)_N + \underbrace{\rho_j\delta_N\left(\mathcal{D}^j_{ij}\right)_P\mathcal{T}^i_j}_{\mathcal{E}}\right], \tag{42}$$

$$(\mathcal{M}_d)_{ij} = -\left(\mathcal{D}^i_{ij}\right)_N, \tag{43}$$

It should be emphasized that the matrix $\mathcal{E}$ (labeled in Eq. (42)) is non-negative due to compressibility effects only. It is reasonable to assume that in general, in regions where diffusion terms are dominant (e.g., near-wall regions), these effects are negligible. Based on this argument, it is reasonable to argue that the leading term of the matrix $(\mathcal{M}_d)_{ii}$ is the matrix $(\mathcal{D}^i_{ij})_N$. Hence, in one dimension, the line entries of the improved implicit diffusive operator matrix ,$\mathcal{M}_d$, when neglecting compressibility effects, have the form of $\{-1, 2, -1\}$. In contrast, in the original UPC scheme, the line entries have the form of $\{-1/2, 3, -1/2\}$. It should be emphasized that the exact discrete Jacobian in the incompressible case is identical to the implicit operator of the improved scheme in the incompressible limit (i.e, also of the form $\{-1, 2, -1\}$). The improved implicit operator in the incompressible limit constitutes a positive definite matrix, but not an M-matrix. Yet, for all practical purposes, the addition of the pseudo-time derivative of the solution vector, to the implicit operator, eliminates this issue, so the improved operator is in fact represented by an M-matrix. Overall, the improved diffusive operator was successfully reconstructed to be closer to the exact discrete Jacobian, while still complying with the positive-preserving scheme. To study the convergence characteristics of the original and improved versions of the turbulence implicit diffusive operator, a numerical simulation of flow about the NACA4412 airfoil at high incidence is performed. Fig. 2 demonstrates the increased efficiency of the improved UPC scheme compared to the original UPC scheme. It can be seen that the use of the improved UPC scheme increases

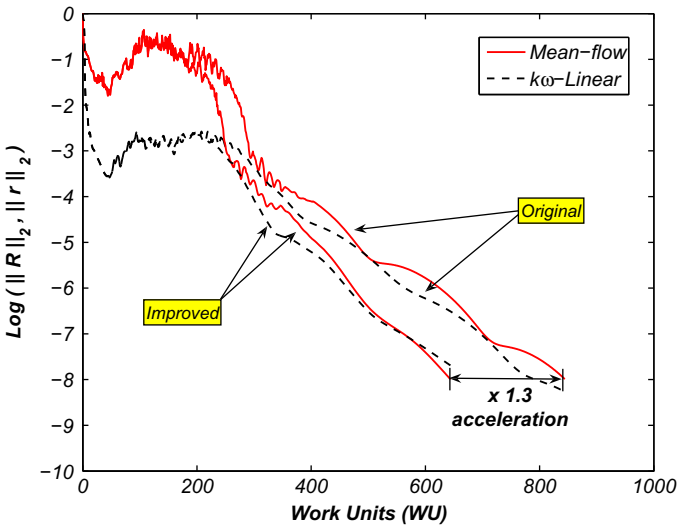

Fig. 2. Comparison of SG convergence histories for simulating flow about the NACA4412 airfoil at $Re_\infty = 1.52 \times 10^6$, $M_\infty = 0.2$, $\alpha = 13.87^\circ$, using a 243×67 C-type grid. Improved UPC (CFL = 400, CFLT = ∞) vs. original UPC (CFL = 400, CFLT = ∞).

the overall efficiency, measured in terms of WU, by a factor of 1.3. It is interesting to note that even though the mean-flow and turbulence equations are integrated in a loosely-coupled manner, use of the improved UPC turbulence equations time-integration scheme also improves the mean-flow equations convergence rate.

In conclusion, the UPC scheme ensures the positivity of turbulence variables, and the stability of numerical time integration of turbulence equations, for any time-step. A further improvement of the scheme with regard to the implicit treatment of turbulence diffusive flux is presented, leading to increased efficiency.

4. Multigrid method

For non-linear equations such as the RANS and turbulence model equation set, the full approximation storage (FAS) multigrid algorithm [35] is mostly used. In multigrid methods, a hierarchy of grids is constructed based on successive coarsening (e.g., elimination of every other grid line, in each direction) of a given fine grid of mesh size h. The resulting grids are of typical mesh sizes $2h$, $4h$, $8h$, etc. Normally, 4 fine-grid cells compose a single underlying coarse grid cell.

The numerical solution is sought on the finest grid in the hierarchy, while the underlying coarse meshes are used to damp low-frequency error modes that can not be efficiently reduced using fine-grid relaxations. Pseudo-time iterations (i.e., Gauss–Seidel relaxation, as described in Sections 3.2.1, 3.2.2) are employed on all grid levels to smooth errors of wavelengths comparable to the corresponding mesh size. As a result, the entire error spectrum is reduced at a comparable rate, leading to notably faster convergence characteristics.

The governing equations, given in integral form in Eq. (18), may be rewritten in operator notation as

$$\frac{\partial}{\partial t}\int_{C_a} \mathcal{Q} dA = \underbrace{-\left[\int_{\partial\Gamma} (\mathcal{H}_c - \mathcal{H}_d) dl - \int_{C_a} \mathcal{S} dA\right]}_{\mathcal{N}(\mathcal{Q})}, \tag{44}$$

where $\mathcal{N}(\mathcal{Q})$ is a non-linear operator representing the RANS and turbulence model equations, operating on the dependent-variable vector $\mathcal{Q}$. The equivalent discrete operator, sampled on a grid of mesh size h, is denoted by $\mathcal{N}^h(\mathcal{Q}^h)$.

4.1. Basic multigrid algorithm

The basic multigrid algorithm employed in this work is based on a *V-cycle* composed of pre-relaxation, restriction, coarse grid correction and post-relaxation (see Fig. 3). Each V-cycle is based on recursively invoking the following two-grid algorithms where h and H denote fine and coarse grid levels, respectively.

4.1.1. Fine-grid pre-relaxation: $\mathcal{N}^h(\overline{\mathcal{Q}}^h) = -\mathcal{R}^h$

Pre-relaxation sweeps are performed on the fine grid to achieve an approximate solution $\overline{\mathcal{Q}}^h$ and a corresponding smooth numerical residual $\mathcal{R}^h$. One or two pre-relaxation sweeps are necessary to ensure that transferred fine-grid defects (residuals) are correctly sampled on coarser grids in the hierarchy, with relatively small aliasing.

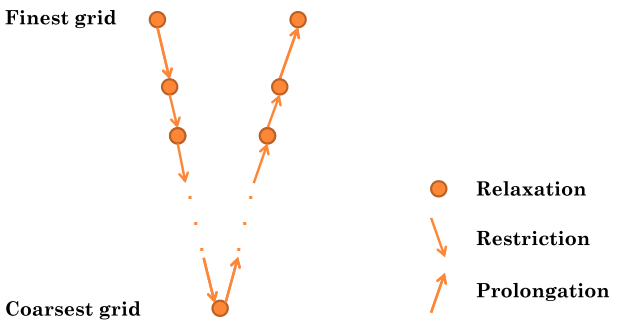

Fig. 3. A schematic description of the V-cycle. Execution proceeds from left to right and top (finest grid) to bottom (coarsest grid) and back up again. On each grid but the coarsest, pre-relaxations are performed prior to transferring (restricting) to the next-coarser grid and post- relaxations are performed after interpolating (prolongating) and adding a coarse grid correction.

4.1.2. Restriction to a coarser grid: $\mathcal{N}^{H}\left(\mathcal{I}_{h}^{H}\mathcal{Q}^{h}\right)-\mathcal{N}^{H}\left(\mathcal{I}_{h}^{H}\overline{\mathcal{Q}}^{h}\right)=\widetilde{\mathcal{I}}_{h}^{H}(\mathcal{R}^{h})$

Using numerical restriction operators, appropriate coarse grid equations are constructed to reduce low-frequency fine-grid errors. An area-weighted restriction operator $\mathcal{I}_{h}^{H}$ is employed to transfer the current fine-grid approximate solution $\overline{\mathcal{Q}}^{h}$ to a coarser grid. The transferred fine-grid residual, $\widetilde{\mathcal{I}}_{h}^{H}(\mathcal{R}^{h})$, is calculated by summing four equivalent fine-grid residuals.

4.1.3. Coarse grid relaxations: $\mathcal{N}^{H}(\overline{\mathcal{Q}}^{H})=\underbrace{\mathcal{N}^{H}(\mathcal{I}_{h}^{H}\overline{\mathcal{Q}}^{h})+\widetilde{\mathcal{I}}_{h}^{H}(\mathcal{R}^{h})}_{\textit{Fine-grid Constants}}-\mathcal{R}^{H}$

The coarse grid equation is solved using local iterations, starting from the initial solution $\bar{\mathcal{Q}}_{0}^{H}=\mathcal{I}_{h}^{H}\overline{\mathcal{Q}}^{h}$. Coarse grid relaxations yield an approximate solution $\bar{\mathcal{Q}}^{H}$, and a corresponding coarse grid residual $\mathcal{R}^{H}$. Note that the first iteration on the coarse grid is driven only by $\widetilde{\mathcal{I}}_{h}^{H}(\mathcal{R}^{h})$, since $\mathcal{N}^{H}(\overline{\mathcal{Q}}_{0}^{H})=\mathcal{N}^{H}(\widetilde{\mathcal{I}}_{h}^{H}\overline{\mathcal{Q}}^{h})$. Note that the first two expressions on the right-hand side of the coarse grid equation, which originate from the fine grid, remain constant throughout coarse grid relaxations.

Numerical tests showed that for this problem, FAS multigrid does not require a direct and most accurate solution on the coarsest grid to ensure efficient acceleration. In fact, attempts to use a large number of iterations in order to achieve an accurate solution on the coarsest grid yield unrealistically large values of turbulent viscosity originating from large initial fine-grid turbulence defects contributing to uncontrolled turbulence production on coarser grids.

4.1.4. Coarse grid correction: $\Delta\overline{\mathcal{Q}}^{h}=\mathcal{I}_{H}^{h}(\overline{\mathcal{Q}}^{H}-\mathcal{I}_{h}^{H}\overline{\mathcal{Q}}^{h})$

The approximate coarse grid solution $\overline{\mathcal{Q}}^{H}$ is transferred (*prolongated*) back to the fine grid, where it is used to correct the current fine-grid solution $\overline{\mathcal{Q}}^{h}$. The prolongation operator is based on bi-linear interpolation. In some cases, straightforward application of turbulence coarse grid corrections may lead to loss of positivity of fine-grid turbulence quantities. This effect arises mainly in the first few near-wall adjacent cells. In this work, a simple positivity-preserving algorithm is applied by an appropriate damping of the coarse grid corrections. Let $\bar{\mathbf{q}}_{i}^{h}$ denote the current turbulence fine-grid solution at cell i, and $\Delta\bar{\mathbf{q}}_{i}^{h}$ denote the coarse grid correction to be applied to that solution. Then, the following algorithm is proposed:

1. If $\bar{\mathbf{q}}_{i}^{h}+\Delta\bar{\mathbf{q}}_{i}^{h}<=0$ then
   (a) If $\bar{\mathbf{q}}_{i}^{h}+\frac{1}{2}\Delta\bar{\mathbf{q}}_{i}^{h}>0$ then
      i. $\Delta\bar{\mathbf{q}}_{i}^{h}=\frac{1}{2}\Delta\bar{\mathbf{q}}_{i}^{h}$

   (b) Else, if $\bar{\mathbf{q}}_{i}^{h}+\frac{1}{4}\Delta\bar{\mathbf{q}}_{i}^{h}>0$ then
      i. $\Delta\bar{\mathbf{q}}_{i}^{h}=\frac{1}{4}\Delta\bar{\mathbf{q}}_{i}^{h}$

   (c) Else
      i. $\Delta\bar{\mathbf{q}}_{i}^{h}=\mathbf{0}$
2. End if
3. $\bar{\mathbf{q}}_{i}^{h}=\bar{\mathbf{q}}_{i}^{h}+\Delta\bar{\mathbf{q}}_{i}^{h}$

Note that the above algorithm is performed separately for both turbulence quantities (ρk and $\rho\omega$), and that damping is always applied to coarse grid corrections of both quantities (regardless of which quantity is examined) to preserve the relation between them, as represented by turbulent viscosity. In addition, it was observed that turbulence coarse grid corrections near boundaries are prone to inaccuracies due to the nature of the turbulence model boundary conditions. To minimize this effect, coarse grid ghost cells are omitted from the stencil of coarse grid cells involved in the interpolation of a CGC. Nevertheless, it is believed that thanks to the fast convergence characteristics of the UPC scheme, the losses of the MG method efficiency due to the CGC damping is minimized. One should bear in mind that for the commonly used two-equation turbulence models (such as the k-ω and the k-ϵ) the turbulence model quantities vary strongly near the wall. Therefore, bi-linear

interpolation may not be sufficiently accurate. Modified interpolations may alleviate this issue by offering better representation of large near-wall gradients (this issue is left for future study).

4.1.5. Fine-grid post-relaxation: $\mathcal{N}^h(\overline{\mathcal{Q}}^h) = -\mathcal{R}^h$

Aside from valuable corrections, application of a coarse grid correction also introduces new errors to the fine-grid solution, arising from interpolation inaccuracies. Several post-iterations are performed to reduce these new errors. In the present work it was found that at least four post-relaxations are required to efficiently reduce the new error components introduced by interpolating and applying a coarse grid correction.

4.2. Cycling strategy

Based on the loosely-coupled time-integration approach used in single-grid solutions, two main multigrid cycling strategies are identified and compared in this work. First, a separated multigrid cycling strategy was considered, based on two cycles (see Fig. 4(a)): A mean-flow cycle where only mean-flow equations are solved while turbulence variables remain frozen, followed by a turbulence cycle where mean-flow variables are frozen and turbulence model equations are solved.

In contrast to separated cycling, combined cycling is based on a single cycle combining both mean-flow and turbulence equations relaxations (see Fig. 4(b)). In a way, such a strategy increases the time-evolution compatibility of the mean-flow and turbulence solutions. Comparisons show that a dramatic increase of up to four times in multigrid efficiency for RANS may be gained by adopting the combined strategy (see Fig. 5). However, since both sets of equations are solved in conjunction on every grid level, combined cycling is considered less stable than the separated cycling alternative. Nevertheless, by

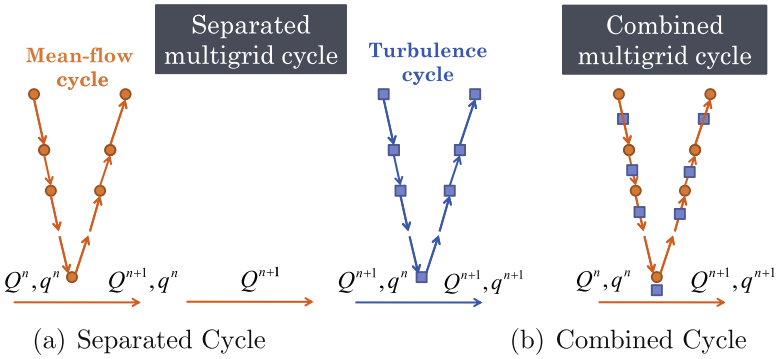

Fig. 4. Multigrid cycling strategies (○ – mean-flow relaxation; □ – turbulence model relaxation).

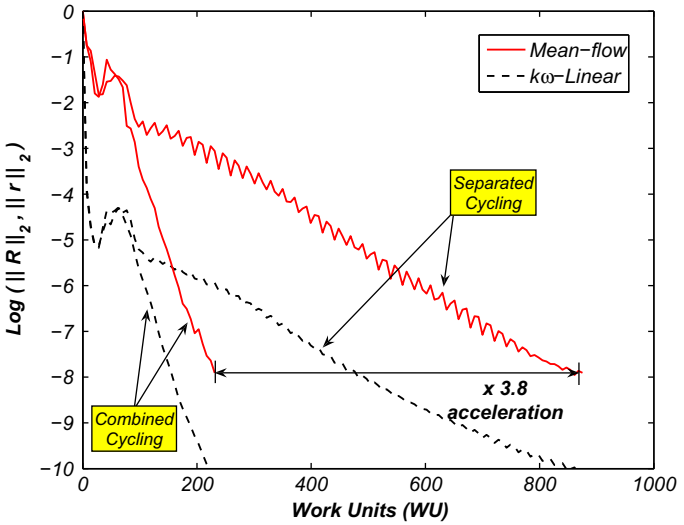

Fig. 5. Comparison of convergence histories of different multigrid cycling strategies for simulating flow about the RAE2822 airfoil at $M_\infty = 0.734$, $Re_\infty = 6.5 \times 10^6$, and $\alpha = 2.54^\circ$ (referred to as case 9 in Ref. [34]).

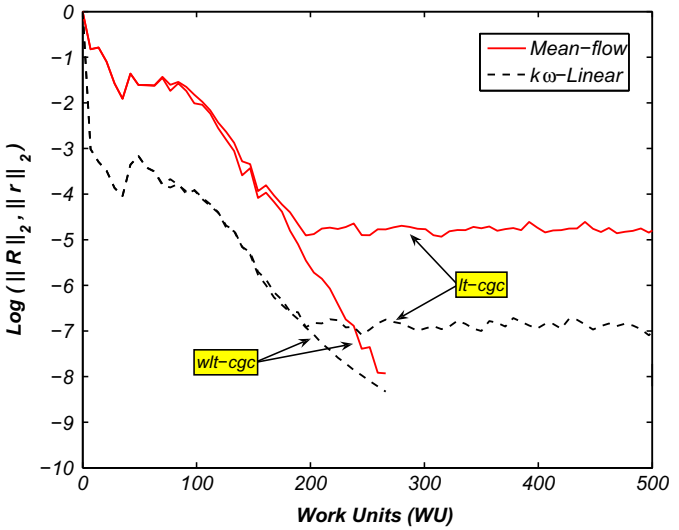

Fig. 6. The effect of turbulence kinetic energy equation coarsest grid correction at the laminar-turbulent transitional boundary layer region on the convergence behavior from flow simulation about the RAE2822 airfoil at $M_\infty = 0.68$, Re_∞, and $\alpha = 1.93^\circ$.

using loosely-coupled time-integration together with the UPC implicit scheme, overall stability is greatly increased, allowing the benefits of combined cycling to be reaped without facing numerical instability or divergence.

4.3. Laminar-turbulent transitional regions in multigrid

A basic requirement of FAS multigrid methods is that the coarse grid resolution would be sufficient to appropriately sample the fine-grid problem. In other words, it is required that all the relevant discrete operators on the coarse grid levels sufficiently resemble the corresponding operators on the fine grid. When it comes to RANS turbulence models this requirement is hard to meet. That is why most FC-MG methods require various artificial stabilizing techniques.

Preliminary numerical experiments show that the present FC-MG method does not require any stabilizing techniques. Still, in a specific region of the flow field, a problem of meeting the coarse-fine-grid operators resemblance requirement is identified. It was found that in the laminar-turbulent transitional boundary layer region, at coarse grid levels, the developed turbulent boundary layer begins at a different location from the one in the fine grid.[1] Moreover, it was observed that the differences in the laminar-turbulent transitional boundary layer starting point affect the mean-flow solution there, which eventually hinders the convergence behavior of the mean-flow equations, as well as that of the turbulence model equations. Numerical experiments showed that the problem did not appear when an extremely fine grid was used. However, such a grid is prohibitively expensive in practice. For any matter of practical use, a simple algorithm is adopted in the present work: once this region is identified, the corresponding coarsest grid turbulence solution correction is dropped to avoid loss of fine-grid accuracy. In particular, this drop was applied to the coarsest grid correction of the turbulence kinetic energy equation only. Fig. 6 shows the convergence behavior of the RANS equations, during simulation of the flow about the RAE2822 airfoil. Two MG simulations using the *kω-Linear* turbulence model were performed: the first included all coarse grid levels corrections, termed hereby *lt-cgc*, while the second simulation neglected the coarsest grid correction of the turbulence kinetic energy equation only, termed hereby *wlt-cgc*. It can be seen from the figure that using the *lt-cgc* strategy, the convergence of the mean-flow and of the turbulence model equations stalls and displays limit-cycle oscillatory behavior. In contrast, using the *wlt-cgc* strategy the convergence was not disturbed. Moreover, it can be seen that prior to the stall point, the convergence pattern using these two strategies is similar.

4.4. Extension of the UPC scheme for multigrid

The original UPC scheme ensures positivity and convergence for time-integration of turbulence model equations in single-grid computations. However, in multigrid, a modification of the UPC scheme is required to retain the positivity of turbulence variables on coarse grid levels as well. On coarse grid levels, forcing terms (transferred fine-grid residuals, and residuals calculated based on the transferred solution) of the turbulence model equations may be regarded as additional source terms. Unless they are appropriately treated they may cause loss of positivity of turbulence variables. Hereafter, an appropriate numerical treatment of these terms is presented, aimed at extending the UPC scheme for use in multigrid methods.

[1] The identification of the transitional location was based on the place where the turbulent viscosity reached the value of the molecular viscosity.

Let $\boldsymbol{n}(\boldsymbol{q})$ denote the non-linear discrete operator representing the turbulence model equations alone, correspondingly operating on the turbulence variables vector $\boldsymbol{q}$ (similar to Eq. (44)). A typical discrete coarse grid equation for the turbulence variables is of the form:

$$\boldsymbol{n}^{\boldsymbol{H}}(\bar{\boldsymbol{q}}^{\boldsymbol{H}}) = \underbrace{\boldsymbol{n}^{\boldsymbol{H}}(\mathcal{I}_{\boldsymbol{h}}^{\boldsymbol{H}}\bar{\boldsymbol{q}}^{\boldsymbol{h}}) + \widetilde{\boldsymbol{I}}_{\boldsymbol{h}}^{\boldsymbol{H}}(\boldsymbol{r}^{\boldsymbol{h}})}_{\textit{forcing term}} - \boldsymbol{r}^{\boldsymbol{H}}, \tag{45}$$

where the forcing term (labeled in Eq. (45)) denoted by

$$\boldsymbol{c}^{\boldsymbol{H}} \equiv [\boldsymbol{c}_{\boldsymbol{k}}, \boldsymbol{c}_{\boldsymbol{w}}] \triangleq \boldsymbol{n}^{\boldsymbol{H}}(\mathcal{I}_{\boldsymbol{h}}^{\boldsymbol{H}}\bar{\boldsymbol{q}}^{\boldsymbol{h}}) + \widetilde{\boldsymbol{I}}_{\boldsymbol{h}}^{\boldsymbol{H}}(\boldsymbol{r}^{\boldsymbol{h}}), \tag{46}$$

is a constant vector. Consequently, the time-marching delta form of the discretized turbulence model equations on the coarse grid level is given in (the index H is hereafter omitted for convenience):

$$\left[\frac{A}{\Delta t}\mathcal{I} + \mathcal{M}\right]^n \Delta\mathbf{q}^n = \mathbf{r}^n - \mathbf{c}. \tag{47}$$

The motivation is to modify the implicit operator to appropriately account for the *new* source term, in the form of vector $\mathbf{c}$. First, the vector $(-\mathbf{c})$ is decomposed to positive and negative parts (based on the scalar decomposition defined in Eq. (34)). The resulting set of equations is

$$\left[\frac{A}{\Delta t}\mathcal{I} + \mathcal{M}\right]^n \Delta\mathbf{q}^n = \mathbf{r}^n + \mathbf{c}_P - \mathbf{c}_N. \tag{48}$$

For the purpose of extending the UPC scheme for use on coarse grid levels, the implicit delta form of Eq. (48) is split and rewritten as follows (assuming $\Delta t \to \infty$):

$$\mathcal{M}^n\mathbf{q}^{n+1} = \mathbf{r}^n + \mathcal{M}^n\mathbf{q}^n + \mathbf{c}_P - \mathbf{c}_N. \tag{49}$$

The stabilizing term originating from discretization of the time derivative is dropped in order to ensure an unconditionally positive-convergent scheme. Bearing in mind that the basic UPC scheme (designed for single-grid computations) ensures that the vector $\mathbf{r}^n + \mathcal{M}^n\mathbf{q}^n$ is non-negative, on coarse grid levels, the presence of the additional constant vector $-\mathbf{c}_N$ may not meet the condition of a non-negative right-hand side of the non-delta form equation, namely that the right-hand side vector of Eq. (49) will be non-negative. By approximating $\mathbf{c}_N$ as

$$\mathbf{c}_N \approx \mathcal{C}\mathbf{q}^{n+1}, \tag{50}$$

where the matrix $\mathcal{C}$ is defined as follows:

$$\mathcal{C} = \begin{bmatrix} \frac{(c_k)_N}{(\rho k)^n} & 0 \\ 0 & \frac{(c_\omega)_N}{(\rho\omega)^n} \end{bmatrix}. \tag{51}$$

Eq. (49) may be recast as

$$[\mathcal{M} + \mathcal{C}]^n\mathbf{q}^{n+1} = \mathbf{r}^n + \mathcal{M}^n\mathbf{q}^n + \mathbf{c}_P. \tag{52}$$

Since the left-hand side matrix, $[\mathcal{M} + \mathcal{C}]$ is also an M-matrix, and since the right-hand side vector of Eq. (52), $\mathbf{r}^n + \mathcal{M}^n\mathbf{q}^n + \mathbf{c}_P$, is non-negative, positivity of the vector $\mathbf{q}^{n+1}$ is unconditionally guaranteed. Finally, the delta form of the extended UPC scheme for coarse grid levels is attained by adding the vector $-\mathcal{C}^n\mathbf{q}^n(\equiv -\mathbf{c}_N)$ to both sides of Eq. (52), and returning the vector $\mathcal{M}^n\mathbf{q}^n$ to its original place on the left-hand side of the equation:

$$\left[\frac{A}{\Delta t}\mathcal{I} + \mathcal{M} + \mathcal{C}\right]^n \Delta\mathbf{q}^n = \mathbf{r}^n - \mathbf{c}. \tag{53}$$

Although, Eq. (53) guarantees positivity and convergence for any time step, in practice it was found that using an infinite time step for the turbulence model equations results in an excessive and unrealistic build-up of turbulent viscosity values on coarse grid levels. This anomaly was mainly noted during early stages of the simulation when the transferred fine-grid defects are still large. However, numerical experiments show that stable simulations can be achieved with a turbulence model CFLT number as high as twice the CFL number that is used for the mean-flow equations. It should be emphasized that realizability constraints [36] that were derived for the basic turbulence model are not adequate for coarse grid levels, since the additional fine-grid defect may be regarded as an additional source or production term, which the basic realizability constraints do not account for. This is believed to be the origin of the excessive build-up of turbulent viscosity on coarse grid levels.

5. Numerical examples

Three well-known test cases are simulated and examined using the proposed multigrid method. The aim of the tests is twofold: first to study the convergence characteristics of the new multigrid algorithm; and second, to verify that the proposed procedure indeed preserves the positivity of the turbulence variables. The first test case is the separated flow about the NACA4412 airfoil at high incidence. The second test is the transonic flow about the RAE2822 airfoil. Internal flow through a plane asymmetric diffuser is the last test case. Several general remarks and definitions should be made prior to proceeding:

- The *convergence* criterion was set to a drop of eight orders in the magnitude of the mean-flow equations residual, compared to the initial residual.
- Convergence was measured in normalized *work units (WU)*, each equal to the computational time that is required to perform a single fine-grid relaxation sweep.
- A uniform CFL number was used on all grid levels of a given simulation. The maximum CFL (as stated in the description of the simulation) was achieved after 10 cycles, or 40 iterations, in multigrid and single-grid simulations, respectively.
- A multigrid hierarchy of 3 grid levels was used in all simulations that were conducted in this work. In addition, a hierarchy of 4 grid levels was used in two of the test cases (marked by "MG 4L").
- It is important to emphasize that in all conducted simulations, no clipping of turbulence variables[2] was employed, nor were there any bounds enforced on turbulence model terms.

5.1. Boundary and initial conditions

Characteristic boundary conditions based on the Riemann invariant are used for the mean-flow equations, and enforced at subsonic inflow and outflow regions. The inflow turbulence kinetic energy is evaluated according to the relation $k = \frac{3}{2}(Tu \cdot U_\infty)^2$ where Tu represents the turbulence intensity. The inflow turbulence dissipation rate is set so that normalized inflow turbulent viscosity is equal to $\mu_{t_\infty} = 0.01$. At the outflow boundary, turbulence variables are extrapolated from interior values. Wall boundary conditions for the turbulence kinetic energy are set to $k = 0$, while the turbulence dissipation rate at the wall is determined following the treatment proposed in Ref. [14]:

$$\omega_{\text{wall}} = CN\frac{19}{9}\frac{6\nu_{\text{wall}}}{\beta(\Delta y_1)^2}, \tag{54}$$

where $CN = 0.1 \times \min[50, \max(10, Re_\infty \Delta y_1 - 20)]$, $Re_\infty \Delta y_1$ is the cell Reynolds number and Δy_1 denotes the distance to the first cell center neighboring the wall, as measured from the wall. The initial solution of the mean-flow equations and of the turbulence model equations is set to uniform free-stream flow throughout the flow field.

5.2. NACA4412 airfoil

Simulation of the flow about a NACA4412 airfoil at high incidence is a well-known test for a solver's ability to accurately resolve high lift separated flows. In the current work, flow about the airfoil at an incidence of $\alpha = 13.87°$, a Mach number of $M_\infty = 0.2$ and a Reynolds number of $Re_\infty = 1.52 \times 10^6$ is simulated using the *kω-Linear* turbulence model, and compared to the experimental results of Ref. [37]. Two different grid topologies were examined: a C-type grid, and an O-type grid. Common grid parameters are given in Table 2.

At experimental flow conditions [37], a steady trailing-edge separation is present. Fig. 7 shows a comparison of calculated stream-wise velocity profiles and experimental data at four stations along the upper airfoil surface (η represents the axis perpendicular to the airfoil surface). The numerical results appear to be in good agreement with the experimental results. Specifically, the velocity profile at the separation region is accurately predicted.

A comparison of convergence histories recorded using the single-grid and multigrid methods is given in Fig. 8, for both the C-type and O-type grids. Note that a 4 level MG hierarchy was also evaluated using the O-type grid. The simulations were conducted with a mean-flow CFL as high as CFL = 400. While the CFL of the turbulence model (CFLT) was as high as CFLT = 800 in multigrid computations, and CFLT $\to \infty$ in single-grid computations. An acceleration factor of two was obtained for tests performed with the C-grid. Moreover, while the SG solver failed to reach convergence using the O-type grid (even with lower CFL and CFLT numbers), the 3 level MG solver converged using the same grid in only 343 work units, corresponding to 53 MG cycles. The 4 level MG solver converged in 312 work units, corresponding to 44 MG cycles. Hence, in this case, further acceleration of 10% is achieved through use of a 4 level MG hierarchy, compared to use of a 3 level MG hierarchy. The similarity of MG performance for both topologies (C-type and O-type grids) indicates the robustness and consistency of the proposed method. Noteworthy is the fact that the convergence characteristics of the mean-flow equations and of the turbulence model equations are similar. Consequently, it is recognized that stability and convergence of the mean-flow equations and of the turbulence model equations are in some sense coupled. This can be realized from the fact that, although these two sets of equations are solved in a loosely-coupled time marching manner, their multigrid cycling is

[2] Except for positive enforcement of coarse grid corrections, as described in Section 4.1.

Table 2
NACA4412 computational grid information.

Grid name	Grid dimension	Far-field	Δy_1	y^+
C-type grid	243×67	14 Chords	5×10^{-6}	$\leqslant 1$
O-type grid	283×95	25 Chords	3×10^{-6}	$\leqslant 0.62$

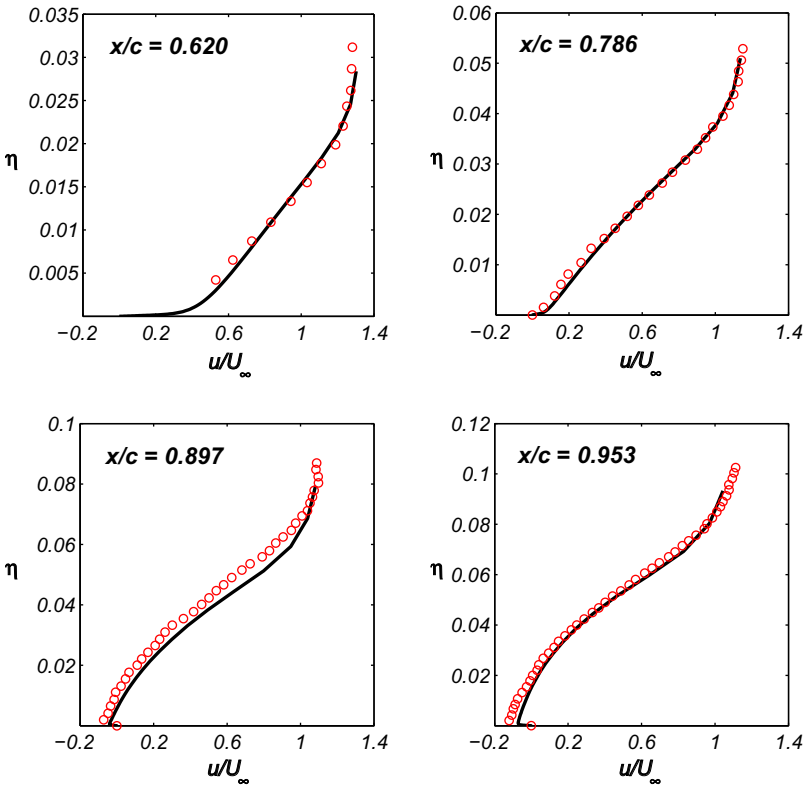

Fig. 7. Comparison between calculated and measured stream-wise velocity profiles at four stations along the upper NACA4412 airfoil surface: ∘, experiment [37], – computation.

strongly coupled. Furthermore, it is well-known that due to the high numerical stiffness of turbulence model equations, turbulent simulations converge slowly as they require the use of smaller time steps along with the need to closely follow the evolution of the simulation. In contrast, the use of the UPC scheme completely overturns the trend. The ability to utilize a very large time step for the turbulence model solver guarantees fast convergence of the turbulence equations, with respect to the current mean-flow state. This is achieved while guaranteeing positivity of turbulence quantities. Thus, apart from stabilizing time-integration of turbulence model equations, use of the UPC scheme also brings about an accelerated convergence of the mean-flow equations as well.

A closer examination of turbulent solutions on all levels of the MG hierarchy is performed to shed further light on the issue of minimal coarse grid level resolution. Throughout the convergence process, the MG coarse grid correction, $\Delta\overline{\mathcal{Q}}^h = \mathcal{I}_H^h(\overline{\mathcal{Q}}^H - \mathcal{I}_h^H\overline{\mathcal{Q}}^h)$, gradually decreases, indicating that coarse level solutions $(\overline{\mathcal{Q}}^H)$ resemble the fine level solution $(\overline{\mathcal{Q}}^h)$. The behavior of turbulent solutions obtained on all grid levels of the MG hierarchy is qualitatively examined through comparison of turbulence viscosity (μ_t) values, shown in Fig. 9. The comparison was based on solutions obtained after 40 MG cycles (nearing convergence) for the NACA4412 airfoil, using the C-type grid. High turbulence viscosity values appear roughly in the same position in the wake on all MG levels, but while maximum values of μ_t on the finest and intermediate levels differ by only 2%, the maximum value on the coarsest level differs by as much as 13% with regards to the finest level maximum. The variation in turbulence viscosity values on different MG levels is mainly related to the increasing loss of resolution on coarse grid levels. Therefore, it is believed that the variance of turbulence viscosity values on coarse grid levels occurs due to gradual loss of accuracy in the approximation of non-linear turbulence model source terms. It is clear that in MG simulations based on more than 3 levels, even larger variations in turbulence viscosity values will occur.

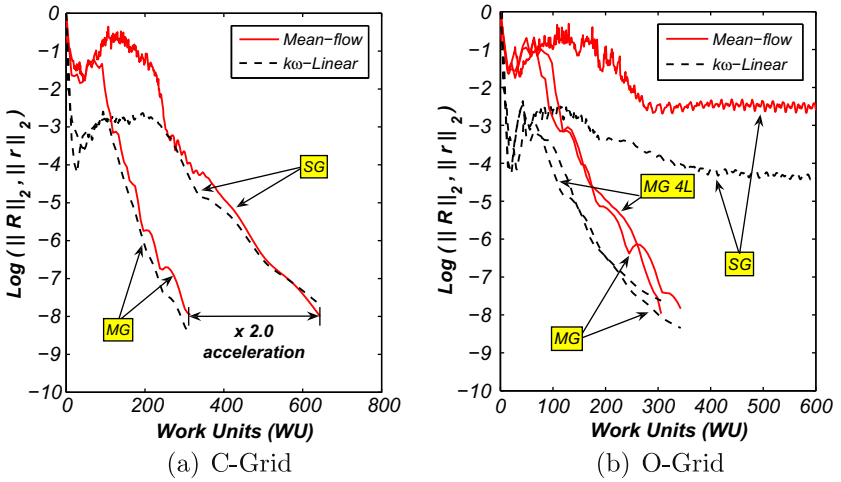

(a) C-Grid (b) O-Grid

Fig. 8. Comparison of convergence histories for the NACA4412 airfoil at $Re_\infty = 1.52 \times 10^6$, $M_\infty = 0.2, \alpha = 13.87^\circ$, MG(CFL = 400,CFLT = 800) vs. SG(CFL = 400,CFLT = ∞).

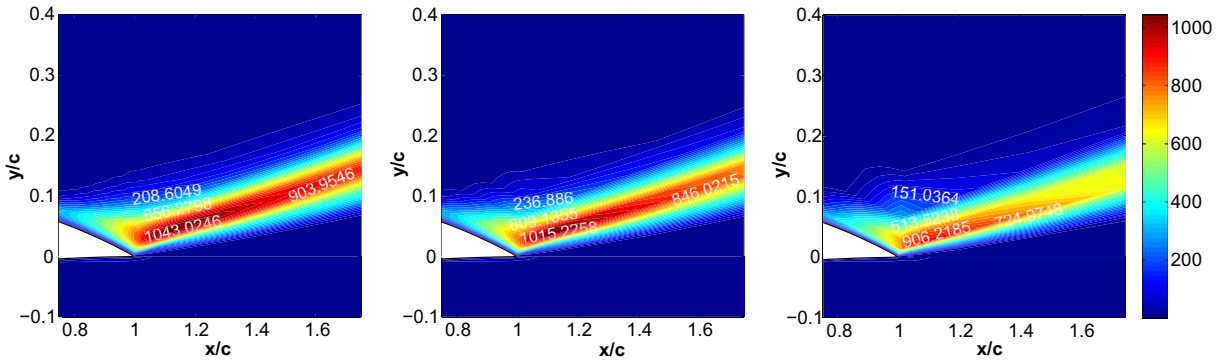

(a) Finest MG Level (b) Intermediate MG Level (c) Coarsest MG Level

Fig. 9. Comparison of turbulence viscosity (μ_t) distributions obtained after 40 cycles (nearing convergence), on different levels of a MG solution for the NACA4412 airfoil at $Re_\infty = 1.52 \times 10^6$, $M_\infty = 0.2$ and $\alpha = 13.87^o$.

5.3. RAE2822 airfoil

The simulation of the transonic flow about the RAE2822 supercritical airfoil is another well-known test case. The experiment performed by Cook et al. [34] covers a wide variety of flow conditions. Two of these flow conditions were simulated using the proposed method, with the *kω-Linear* and *kω-EARSM* turbulence models:

- Mach number, $M_\infty = 0.68$; Reynolds number, $Re_\infty = 6.5 \times 10^6$; and an incidence angle of $\alpha = 1.93^\circ$ (referred to as case 1 in Ref. [34]).
- Mach number, $M_\infty = 0.734$; Reynolds number, $Re_\infty = 6.5 \times 10^6$; and an incidence angle of $\alpha = 2.54^\circ$ (referred to as case 9 in Ref. [34]).

Two C-type grids were employed in the current test: a fine grid, and a coarser grid. Common grid parameters are given in Table 3.

A comparison of the calculated surface pressure coefficient with the experimental data [34] is displayed in Fig. 10(a) for case 1 flow, and in Fig. 10(b) for case 9 flow. The overall agreement between computational and experimental data is very good for both the *kω-Linear* and *kω-EARSM* turbulence models. Specifically, the shock wave location (case 9) is accurately captured.

Comparisons of convergence histories recorded using the single-grid and multigrid methods (both using the UPC scheme), with the *kω-Linear* turbulence model, are presented in Figs. 11 and 12 for case 1 and case 9 flows, respectively. The simulations were conducted with a maximum mean-flow CFL = 200. While the CFL of the turbulence model (CFLT)

Table 3
RAE2822 computational grid information.

Grid name	Grid dimension	Far-field	Δy_1	y^+
Coarse grid (C)	275×67	31 Chords	5×10^{-6}	$\leqslant 1.9$
Fine grid (C)	435×123	23 Chords	1×10^{-6}	$\leqslant 0.43$

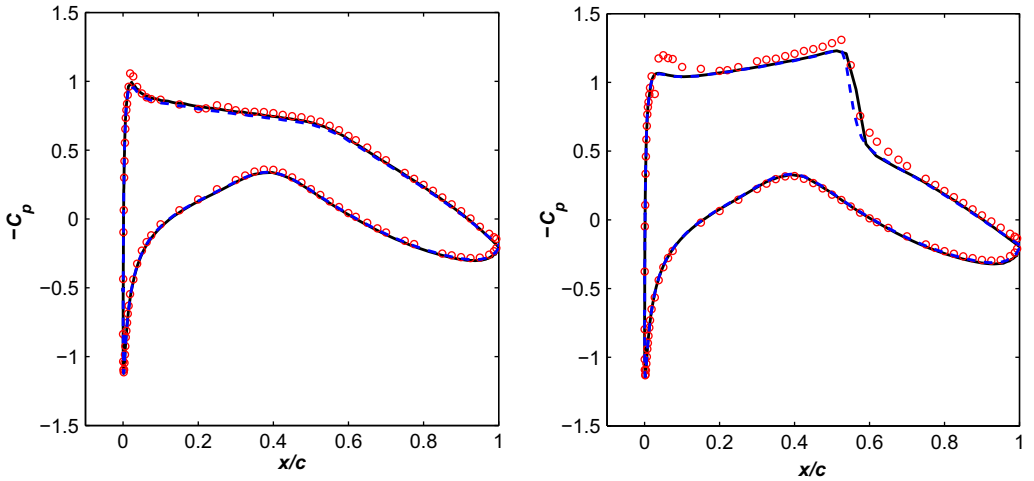

Fig. 10. Comparison between C_p distributions on the RAE2822 airfoil; ∘, experiment [34]; - - -, computation with *kω-EARSM* turbulence model (fine grid); —, computation with *kω-Linear* turbulence model (fine grid).

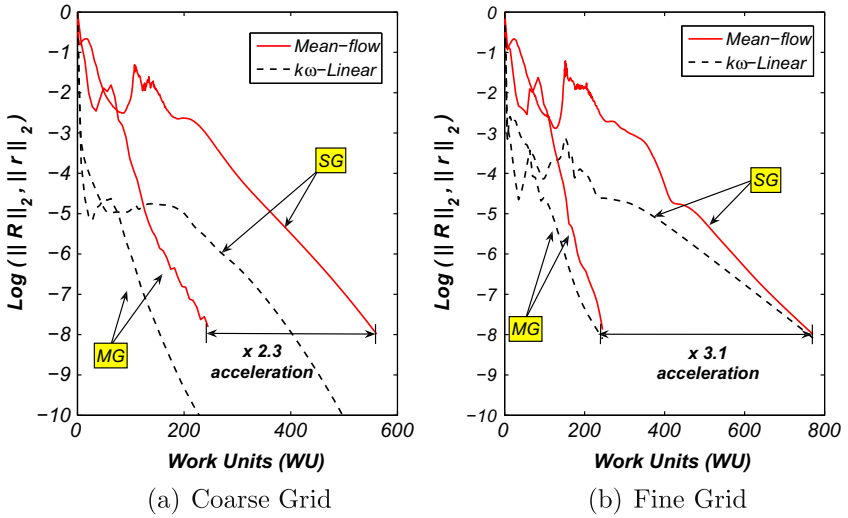

Fig. 11. Comparison of convergence histories obtained using the *kω-Linear* turbulence model for the RAE2822 airfoil at $M_\infty = 0.68$, $Re_\infty = 6.5 \times 10^6$, and $\alpha = 1.93^\circ$ (referred to as case 1 in Ref. [34]), MG(CFL = 200, CFLT = 400) vs. SG(CFL = 200, CFLT = ∞).

was as high as CFLT = 400 in multigrid computations, and CFLT → ∞ in single-grid computations. Note that a 4 level MG hierarchy was also evaluated using the fine grid, for case 9 flow. For case 1 flow, acceleration factors of more than two, and more than three, are obtained using the coarse and fine grids, respectively. Strong evidence as to the robustness of the proposed MG algorithm can also be seen by noting that 3 level MG converges for case 9 flow on the two examined grids in 245 and 357 work units (corresponding to 38 and 51 cycles) for the coarse and fine grid, respectively. On the other hand, single-grid simulations yielded slower convergence using the fine grid than that achieved with the coarse grid, as expected. The 4 level MG solver converged in 291 work units for case 9 flow on the fine grid, corresponding to 41 MG cycles. Hence, in this case,

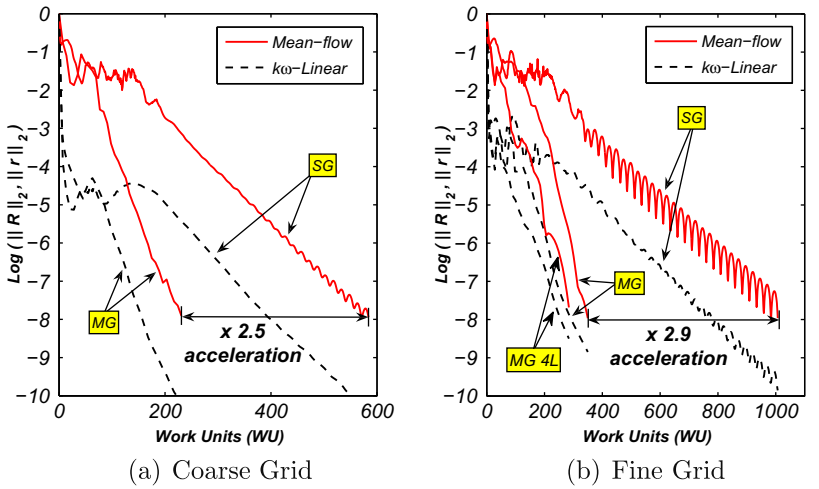

(a) Coarse Grid (b) Fine Grid

Fig. 12. Comparison of convergence histories obtained using the *kω-Linear* turbulence model for the RAE2822 airfoil at $M_\infty = 0.734$, $Re_\infty = 6.5 \times 10^6$, and $\alpha = 2.54°$ (referred to as case 9 in Ref. [34]), MG(CFL = 200, CFLT = 400) vs. SG(CFL = 200, CFLT = ∞).

further acceleration of 18% is achieved through use of a 4 level MG hierarchy, compared to use of a 3 level MG hierarchy. Similar performance is exhibited by the MG algorithm for case 1 flow as well. In addition, it can be seen that SG computations on the fine-grid suffer from noticeable convergence oscillations, while MG convergence remains smooth.

Comparisons of convergence histories obtained using the SG and MG methods, with the *kω-EARSM* turbulence model, on the coarse RAE2822 grid are presented in Fig. 13(a) and (b) for case 1 and case 9 flows, respectively. While a maximum CFL = 200 and CFLT = 400 were allowed in multigrid computations, only CFL = 50 and CFLT = 100 were allowed in single-grid computations. Acceleration factors of nearly two are achieved using the MG method, with respect to an equivalent SG simulation, for case 1 and case 9 flow conditions.

The robustness of the proposed FC-MG-UPC method is once again shown in the fact that its suitable for both the non-linear (EARSM) turbulence model, as well as for the linear turbulence model, without requiring unique numerical treatment or stabilization fixes for any of the models. In addition, it should be noted that use of the proposed method also provides similar acceleration factors for both turbulence models examined in this work, with respect to an equivalent SG method.

5.3.1. Positivity of turbulence quantities

To demonstrate the positivity of turbulence quantities throughout the simulation, a plot of their minimum value histories in all three grid levels of the MG hierarchy is presented in Fig. 15 for flow simulation about the RAE2822 airfoil at case 9 flow conditions, using the *kω-Linear* turbulence model and the coarse grid. It can be seen that no negative values appear

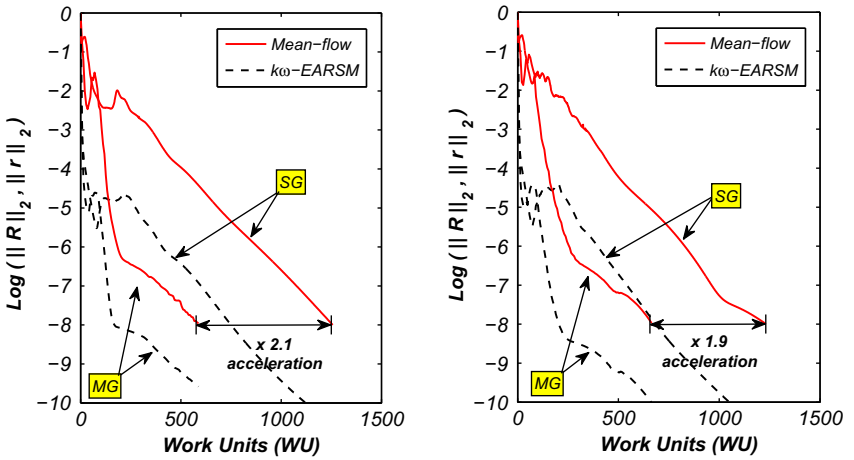

(a) Case 1 Flow (b) Case 9 Flow

Fig. 13. Comparison of convergence histories obtained using the *kω-EARSM* turbulence model for the RAE2822 airfoil at different flow conditions, MG(CFL = 200, CFLT = 400) vs. SG(CFL = 50, CFLT = 100).

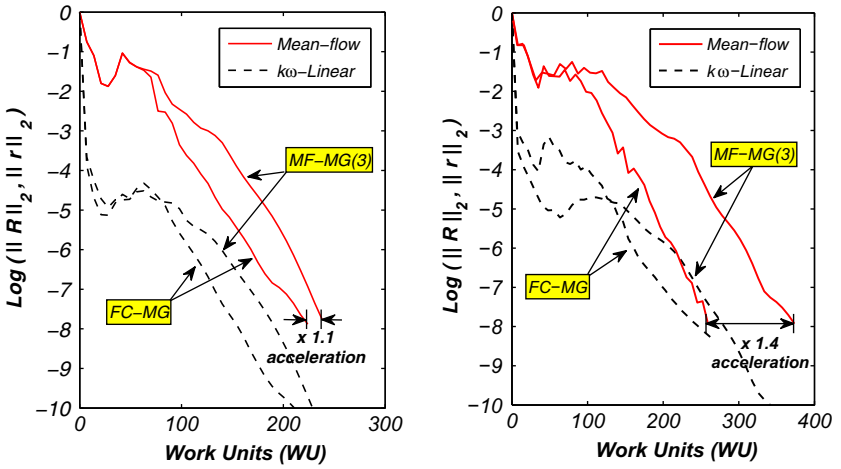

Fig. 14. Comparison of convergence histories for the RAE2822 airfoil at $M_\infty = 0.734$, $Re_\infty = 6.5 \times 10^6$, and $\alpha = 2.54°$ (referred to as case 9 in Ref. [34]), FC-MG (CFL = 200, CFLT = 400) vs. MF-MG(CFL = 200,170 CFLT = 400,340).

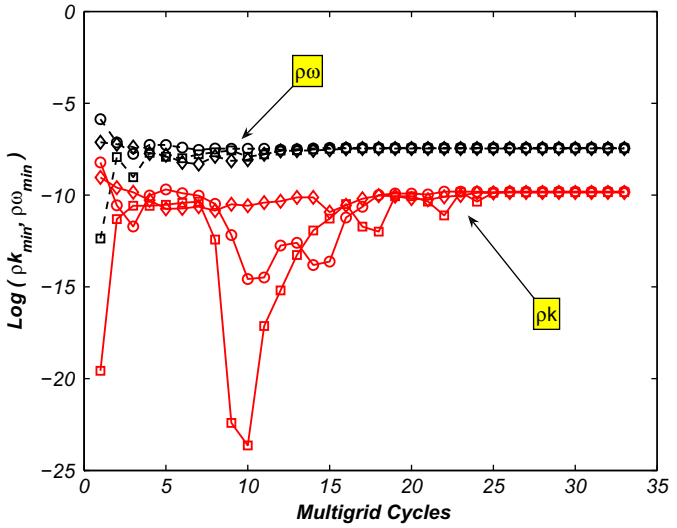

Fig. 15. Turbulence quantities minima throughout a multigrid simulation of case 9 flow about the RAE2822 airfoil, using the *kω-Linear* turbulence model and a coarse grid: ◇, finest grid level; □, intermediate grid level; ○, coarsest grid level.

throughout the entire simulation, and that towards convergence, minima of turbulence quantities also converge to practically the same value at all grid levels.

5.3.2. Mean-flow multigrid (MF-MG)

As mentioned in the Introduction, the mean-flow multigrid (MF-MG) approach is commonly used to bypass numerical difficulties arising from the destabilizing effects of productive turbulence model source terms. However, insufficient acceleration of the turbulence transport equations due to a partial use of single-grid computations in MF-MG may result in an overall reduced convergence rate, compared to fully-coupled multigrid. To evaluate the performance of the proposed FC-MG-UPC method, with regards to the MF-MG approach, a comparison of convergence histories was performed. To bridge the gap in the time evolution of the turbulent solution, as compared to the mean-flow solution obtained in MF-MG, 3 relaxations of turbulence model equations were performed for every mean-flow relaxation on the fine-grid level. This was found to be crucial for ensuring the stability of MF-MG. Comparisons of convergence histories obtained using the proposed fully-coupled multigrid method (FC-MG-UPC) and MF-MG for simulating case 9 flow on the coarse and fine RAE2822 grids, using the *kω-Linear* turbulence model, are shown in Fig. 14(a) and (b), respectively. It should be emphasized that while the FC-MG-UPC allowed use of CFL = 200 for the fine RAE2822 grid, the MF-MG approach converged only using a lower CFL = 170. The

comparison suggests that the FC-MG-UPC method is favorable to the MF-MG approach in terms of robustness and efficiency. This is believed to be related to insufficient acceleration of the turbulence transport equations due to partial use of single-grid computations in MF-MG.

5.4. Plane asymmetric diffuser

Computations of the steady turbulent flow through a plane asymmetric diffuser, schematically shown in Fig. 16, have been conducted. The long inlet channel (110 times of the channel height), followed by a diffuser with an opening angle of 10° of the bottom wall with an expansion ratio of 4.7. The outlet boundary is placed at the position of $x = 105H$. The plane

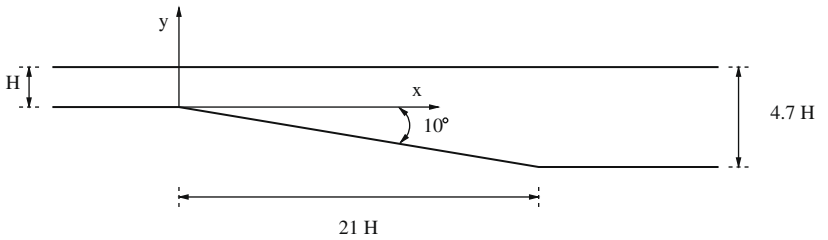

Fig. 16. Schematic description of the plane asymmetric diffuser geometry.

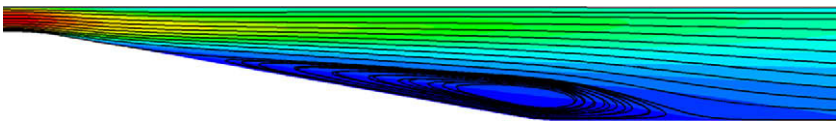

Fig. 17. Streamlines and stream-wise velocity map of the plane asymmetric diffuser.

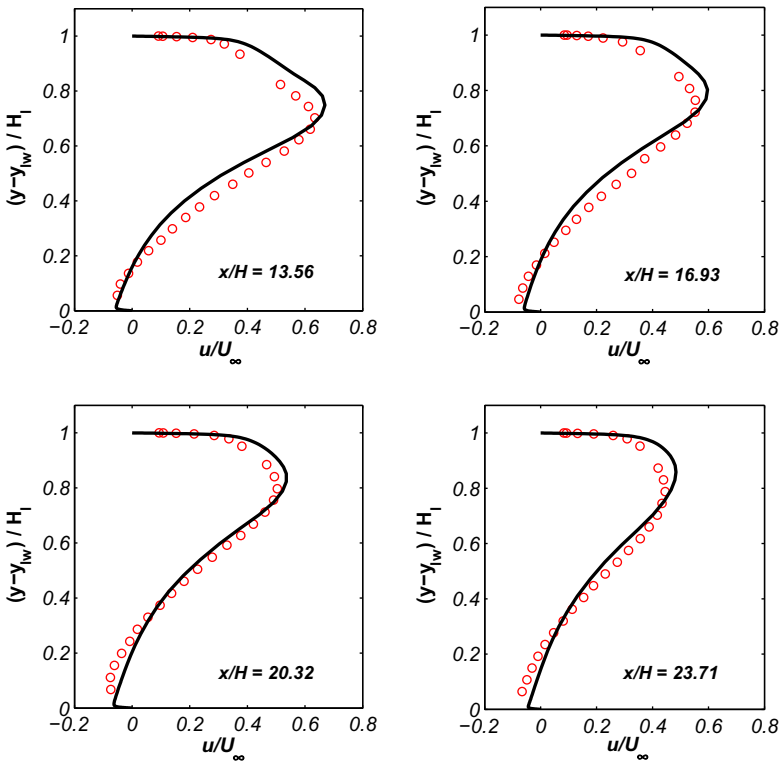

Fig. 18. Comparison between calculated and measured stream-wise velocity profiles at four stations along the plane asymmetric diffuser: ○, experiment [38], —, computation (y_{lw} – coordinates of lower wall in the y axis, H_l – local diffuser height).

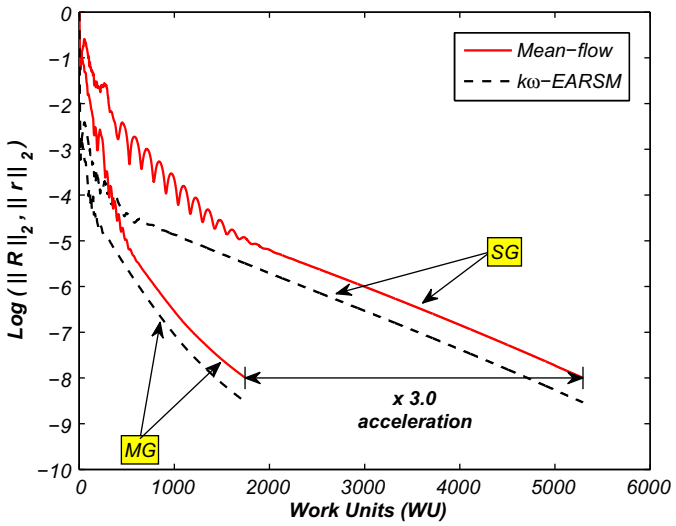

Fig. 19. Comparison of convergence histories obtained using the $k\omega$-*EARSM* turbulence model for the plane asymmetric diffuser at $M_\infty = 0.2$ and $Re_\infty = 2 \times 10^4$, MG(CFL = 300, CFLT = 300) vs. SG(CFL = 300, CFLT = 300).

asymmetric diffuser geometry was selected according to the experimental study performed by Buice and Eaton [38]. In this work, the inlet Mach number was set to $M_\infty = 0.2$ and the reference Reynolds number that is based on the channel height and the inlet velocity is $Re_\infty = 2 \times 10^4$. The computational grid has the dimension of 419×113 where the first grid point neighboring the walls is placed at a distance of 3×10^{-4} of the channel height, corresponding to $y^+ \leqslant 0.35$.

The experimental flow conditions and diffuser geometry are characterized by a smooth adverse pressure gradient driven separation on the bottom inclined wall (see Fig. 17). In the diffuser used in the experiment, the diffuser upstream and downstream bottom inclined wall corners were rounded to prevent separation at this corners. Internal turbulent flow simulation of geometries where separation is not ruled by sharp corners is very challenging, particularly the separation point location and the extent of the recirculation region. Past numerical studies [39,40] suggest that advanced turbulence models may have an advantage in flow prediction in such cases. Therefore the $k\omega$-*EARSM* model is used for this test case.

A comparison of the calculated stream-wise velocity profile and experimental data at four stations along the separation region is shown in Fig. 18. The computed results are in reasonable agreement with the experimental data.

A comparison of convergence histories recorded using the single-grid and the proposed FC-MG-UPC methods is shown in Fig. 19. The simulations were conducted with a uniform CFL number for the mean-flow and turbulence model equations: CFL = CFLT = 300. An acceleration factor of three was obtained using the proposed MG method, as compared to an equivalent SG solution. Furthermore, while SG convergence exhibits an oscillatory pattern at early stages of the simulation, the convergence pattern using the MG method is smoother by far.

6. Summary

A robust multigrid method for the solution of RANS equations with two-equation turbulence models is presented. The method employs a basic relaxation scheme (alternating line Gauss–Siedel) where mean-flow and turbulence model equations are marched in time in a loosely-coupled manner. Two pillars stand at the base of the proposed MG method: use of an extended version of the unconditionally positive-convergent scheme for two-equation turbulence models, adapted for use in multigrid, and the use of a strongly coupled multigrid cycling strategy. It is shown that, by using the UPC scheme in single-grid computations alone, convergence rates of the overall flow solver are increased nearly five times compared to a solver based on a standard implicit scheme for turbulence model equations. In addition, convergence characteristics of the UPC scheme have been further improved thanks to modification of the diffusive implicit operator.

Moreover, favoring the use of a combined multigrid cycling strategy over a separated strategy nearly quadrupled the overall efficiency, as measured by computational WU required for convergence. It was also found that the fully coupled (FC-MG) approach is favorable to the MF-MG approach in terms of robustness and efficiency. Minimal stabilization in the form of damping of turbulence equations coarse grid corrections was found to be necessary in order to ensure the positivity of turbulence quantities. Specifically, coarsest grid corrections of the turbulence kinetic energy equation were not applied inside laminar-turbulent transitional regions only, and positivity-preserving relaxation of turbulent coarse grid correction was applied, mainly in small near-wall regions. The resulting MG method, termed FC-MG-UPC, is suitable for robust simulations of a wide range of flows thanks to being nearly free of artificial stabilization techniques, and user-supplied parameters.

Numerical experiments showed that the proposed FC-MG-UPC method increases the efficiency compared to an equivalent single-grid method based on the UPC scheme by a factor of up to three. Moreover, the method has proven to be more stable than an equivalent SG-based method, allowing the use of higher CFL numbers for the mean-flow equations and even rapid convergence in a case where the SG-based method failed to converge. Thanks to the added stability gained by the use of the UPC scheme, a uniform CFL number and second order spatial accuracy could be used on all grid levels of the MG hierarchy. Moreover, the robustness of the proposed FC-MG-UPC method is well reflected by its impressive performance with the non-linear, EARSM, turbulence model, which is considered to be more numerically stiff than linear models.

Acknowledgment

The authors would like to thank Dr. Yuval Levy for his valuable comments.

References

[1] D.C. Wilcox, Turbulence Modeling for CFD, second ed., DCW Industries, Inc, 5354 Palm Drive, La Canada, CA 91011, 1998.
[2] B.E. Launder, B.I. Sharma, Application of the energy-dissipation model of turbulence to the calculation of flow near a spinning disc, Letters in Heat and Mass Transfer 1 (1974) 131–138.
[3] Z.-N. Wu, S. Fu, Positivity of *k*-epsilon turbulence models for incompressible flow, Mathematical Models and Methods in Applied Sciences 12 (3) (2002) 393–406.
[4] I. Yavneh, Why multigrid methods are so efficient, Computing in Science & Engineering 8 (6) (2006) 12–22.
[5] W. Briggs, S. McCormick, A Multigrid Tutorial, Society for Industrial Mathematics, 2000.
[6] U. Trottenberg, C. Oosterlee, A. Schuller, Multigrid–2001, Academic Press, San Diego, 2001.
[7] A. Brandt, Barriers to Achieving Textbook Multigrid Efficiency (TME) in CFD, Institute for Computer Applications in Science and Engineering, NASA Langley Research Center, 1998.
[8] G.A. Gerolymos, I. Vallet, Mean-flow-multigrid for implicit Reynolds-stress-model computations, AIAA Journal 43 (9) (2005) 1887–1898.
[9] G.A. Gerolymos, I. Vallet, Implicit meanflow-multigrid algorithms for Reynolds stress model computation of 3-D anisotropy-driven and compressible flows, International Journal for Numerical Methods in Fluids 61 (2008) 185–219.
[10] R.C. Swanson, C.C. Rossow, An efficient flow solver with a transport equation for modeling turbulence, in: 19th AIAA Computational Fluid Dynamics, San-Antonio, Texas, 2009.
[11] J. Fassbender, Robust and efficient computation of turbulent flows around civil transport aircraft at flight Reynolds numbers, Aerospace Science and Technology 9 (8) (2005) 672–680.
[12] P. Walsh, T. Pulliam, The effect of turbulence model solution on viscous flow problems, in: 39th AIAA Aerospace Sciences Meeting & Exhibit, Reno, NV, 2001, AIAA – 2001-1018.
[13] P. Gerlinger, H. Mobus, D. Bruggemann, An implicit multigrid method for turbulent combustion, Journal of Computational Physics 167 (2) (2001) 247–276.
[14] S. Park, J. Kwon, Implementation of *k*-ω turbulence models in an implicit multigrid method, AIAA Journal 42 (2004) 1348–1357.
[15] F. Lin, F. Sotiropoulos, Strongly-coupled multigrid method for 3-d incompressible flows using near-wall turbulence closures, Journal of Fluids Engineering 119 (1997) 314.
[16] M. Vazquez, M. Ravachol, F. Chalot, M. Mallet, The robustness issue on multigrid schemes applied to the Navier–Stokes equations for, laminar turbulent incompressible and compressible flows, International Journal for Numerical Methods in Fluids 45 (5) (2004) 555–579.
[17] P. Gerlinger, D. Brüggemann, Multigrid convergence acceleration for turbulent supersonic flows, International Journal for Numerical Methods in Fluids 24 (10) (1997) 1019–1035.
[18] P. Gerlinger, D. Brüggemann, An implicit multigrid scheme for the compressible Navier–Stokes equations with low-Reynolds-number turbulence closure, Journal of Fluids Engineering 120 (1998) 257.
[19] T. Park, Multigrid method and low-Reynolds-number *k*-ϵ model for turbulent recirculating flows, Numerical Heat Transfer Part B: Fundamentals 36 (4) (1999) 433–456.
[20] X. Zheng, C. Liao, C. Liu, C. Sung, T. Huang, Multigrid computation of incompressible flows using two-equation turbulence models: part I – numerical method, Journal of Fluids Engineering 119 (1997) 893–900.
[21] P. Gerlinger, P. Stoll, D. Brüggemann, Robust implicit multigrid method for the simulation of turbulent supersonic mixing, AIAA Journal 37 (6) (1999) 766–768.
[22] P. Gerlinger, An evaluation of multigrid methods for the simulation of turbulent combustion, in: 17th AIAA Computational Flow Dynamics Conference, 2005, pp. 1–14.
[23] J. Wackers, B. Koren, Multigrid solution method for the steady RANS equations, Journal of Computational Physics 226 (2) (2007) 1784–1807.
[24] J. Yan, F. Thiele, L. Xue, A modified full multigrid algorithm for the Navier–Stokes equations, Computers and Fluids 36 (2) (2007) 445–454.
[25] Y. Mor-Yossef, Y. Levy, Unconditionally positive implicit procedure for two-equation turbulence models: Application to *k*-ω turbulence models, Journal of Computational Physics 220 (1) (2006) 88–108.
[26] Johan C. Kok, Resolving the dependence on freestream values for the *k*-ω turbulence model, AIAA Journal 38 (7) (2000) 1292–1295.
[27] S. Wallin, A. Johansson, An explicit algebraic Reynolds stress model for incompressible and compressible turbulent flows, Journal of Fluid Mechanics 43 (2000) 89–132.
[28] P. Batten, M.A. Leschziner, U.C. Goldberg, Average-state Jacobians and implicit methods for compressible viscous and turbulent flows, Journal of Computational Physics 137 (1) (1997) 38–78.
[29] G.D. van Albada, B. van Leer, W.W. Roberts, A comparative study of computational methods in cosmic gas dynamics, Astronomy and Astrophysics 108 (1) (1982) 76–84.
[30] P. Jawahar, H. Kamath, A high-resolution procedure for Euler and Navier–Stokes computations on unstructured grids, Journal of Computational Physics 164 (1) (2000) 165–203.
[31] E.F. Toro, Riemann Solvers and Numerical Methods for Fluid Dynamics: a Practical Introduction, second ed., Springer-Verlag, Berlin, Heidelberg, 1999.
[32] A. Berman, R.J. Plemmons, Nonnegative Matrices in the Mathematical Sciences, Computer Science and Applied Mathematics, Academic Press, Inc., New York, 1979.
[33] Y. Mor-Yossef, Y. Levy, The unconditionally positive-convergent implicit time integration scheme for two-equation turbulence models: revisited, Computers & Fluids 38 (10) (2009) 1984–1994.
[34] P.H. Cook, M.A. McDonald, M.C.P. Firmin, Aerofoil RAE2822-Pressure Distributions, Boundary Layer and Wake Measurements, Technical Report: AR 138, AGARD, 1979.
[35] A. Brandt, Multi-level adaptive solutions to boundary-value problems, Mathematics of Computations 31 (138) (1977) 333–390.
[36] U. Schumann, Realizability of Reynolds-stress turbulence models, Physics of Fluids 20 (1977) 721–725.

[37] D. Coles, A.J. Wadcock, Flying-hot-wire study of flow past an NACA4412 airfoil at maximum lift, AIAA Journal 17 (4) (1979) 321–329.
[38] C.U. Buice, J.K. Eaton, Experimental investigation of flow through an asymmetric plane diffuser, Journal of Fluid Engineering 122 (2) (2000) 433–435.
[39] D.D. Apsley, M.A. Leschziner, Advanced turbulence modelling of separated flow in a diffuser, Flow Turbulence and Combustion 63 (1999) 81–112.
[40] P.A. Durbin, Separated flow computations with the k-ϵ-v^2 model, AIAA Journal 33 (4) (1995) 659–664.